

QUANTIFYING THE EFFECT OF FLOW RATE CONTROLLERS ON LIQUID
STEEL FLOW IN CONTINUOUS CASTING MOLD USING CFD MODELING

A THESIS SUBMITTED TO
THE GRADUATE SCHOOL OF NATURAL AND APPLIED SCIENCES
OF
MIDDLE EAST TECHNICAL UNIVERSITY

BY

KADİR ALİ GÜRSOY

IN PARTIAL FULFILLMENT OF THE REQUIREMENTS
FOR
THE DEGREE OF MASTER OF SCIENCE
IN
MECHANICAL ENGINEERING

SEPTEMBER 2014

Approval of the thesis:

**QUANTIFYING THE EFFECT OF FLOW RATE CONTROLLERS ON
LIQUID STEEL FLOW IN CONTINUOUS CASTING MOLD USING CFD
MODELING**

submitted by **KADİR ALİ GÜR SOY** in partial fulfillment of the requirements for the degree of **Master of Science in Mechanical Engineering Department, Middle East Technical University** by,

Prof. Dr. Canan Özgen
Dean, Graduate School of **Natural and Applied Sciences**

Prof. Dr. Suha Oral
Head of Department, **Mechanical Engineering**

Assoc. Prof. Dr. Mehmet Metin Yavuz
Supervisor, **Mechanical Engineering Dept., METU**

Examining Committee Members:

Asst. Prof. Dr. Merve Erdal
Mechanical Engineering Dept., METU

Assoc. Prof. Dr. Mehmet Metin Yavuz
Mechanical Engineering Dept., METU

Asst. Prof. Dr. Cüneyt Sert
Mechanical Engineering Dept., METU

Asst. Prof. Dr. Yiğit Yazıcıoğlu
Mechanical Engineering Dept., METU

Assoc. Prof. Dr. Murat Kadri Aktaş
Mechanical Engineering Dept., TOBB ETU

Date: 03.09.2014

I hereby declare that all information in this document has been obtained and presented in accordance with academic rules and ethical conduct. I also declare that, as required by these rules and conduct, I have fully cited and referenced all material and results that are not original to this work.

Name, Last name : Kadir Ali GÜRSOY

Signature :

ABSTRACT

QUANTIFYING THE EFFECT OF FLOW RATE CONTROLLERS ON LIQUID STEEL FLOW IN CONTINUOUS CASTING MOLD USING CFD MODELING

Gürsoy, Kadir Ali

M.S., Department of Mechanical Engineering

Supervisor: Assoc. Prof. Dr. Mehmet Metin Yavuz

September 2014, 83 pages

Continuous casting of steel is accepted to operate most efficient when all its aspect are in steady state conditions. Transport rate of molten steel from tundish to the caster mold is among the parameters desired to be constant. In this process, the flow through tundish to the mold can be controlled by several flow rate control mechanism including stopper rods and slide gates. Ladle change operations in continuous casting machines result in liquid steel level changes in tundishes. During this transient event of production, the flow rate controller opening is increased to reduce the pressure drop across the opening, which helps to keep the mass flow rate constant for the reduced liquid steel level in tundish. In literature there is lack of research studies related to the influence of flow controller type on mold flow structure.

The present study investigates the mold flow structure at constant throughput condition for different slide gate and stopper rod openings by utilizing computational fluid dynamic (CFD) modeling. Detailed validation of the CFD models are conducted using available experimental data and the performances of three different turbulence models, standard k- ϵ , realizable k- ϵ and k- ω SST are compared. The simulations are performed with ANSYS Fluent. The constant throughput casting operations for different slide

gate and stopper rod controller openings are simulated to quantify the effect of both flow controller and their opening level on mold flow, particularly the meniscus region. The results indicate that for a slide gate controlled system, the meniscus velocities are significantly affected by the changes in the opening level. The steady state operations, specified as constant throughput casting, do not provide the same mold flow if the slide gate opening is altered. On the other hand, for the stopper rod controlled system the stopper rod opening level changes do not affect the meniscus velocities and the flow structures within the mold.

Keywords: Mold flow, Continuous casting of steel, CFD, Turbulence modeling, Flow controller, Slide gate, Stopper rod.

ÖZ

AKIŞ KONTROLCÜLERİNİN SÜREKLİ KALIP İÇİ SIVI ÇELİK DÖKÜMÜNE ETKİSİNİN HAD MODELLEMESİ İLE BELİRLENMESİ

Gürsoy, Kadir Ali

Yüksek Lisans, Makina Mühendisliği Bölümü

Tez Yöneticisi: Doç. Dr. Mehmet Metin Yavuz

Eylül 2014, 83 sayfa

Süreklî sıvı çelik dökümünün, bütün parametreleri durağan durumdayken en verimli olarak çalıştığı kabul edilmiştir. Erimiş çeliğin tandiştten döküm kalıbına transfer hızının da sabit olması istenmektedir. Bu işlemde tandiştten kalıba doğru olan akış, durdurucu bar ve kayar kapı gibi çeşitli akış kontrol mekanizmaları tarafından kontrol edilebilir. Döküm makinalarında kova değişim işlemleri tandişlerde sıvı çelik düzeylerinin değişimine sebep olur. Bu geçici üretim olayı sırasında, akış kontrolcüsünün açıklığı artırılarak, tandişte düşen sıvı çelik düzeyinden dolayı açıklıkta oluşan basınç düşmesi azaltılmaya ve kütle akış hızı sabit düzeyde tutulmaya çalışılmaktadır. Literatürde akış kontrolcüsünün kalıp içi akış yapısına etkisini inceleyen yeterli çalışma bulunmamaktadır.

Mevcut çalışma kalıp içi akışın sabit döküm şartlarındaki yapısını değişik kayar kapı ve durdurucu bar açıklıklarına göre değişimini hesaplamalı akışkanlar dinamiğinden (HAD) modellemesi yararlanarak incelemektedir. HAD modellerinin detaylı ispatı mevcut deneysel datalarla kıyaslanarak yapılmıştır ve üç türbülans modelinin, standard k- ϵ , realizable k- ϵ and k- ω SST, performansları kıyaslanmıştır. Simülasyonlar ANSYS Fluent kullanılarak yapılmıştır. Simülasyonlar sabit hacimli döküm

operasyonunda farklı akış kontrolcülerinin ve kontrolcü açıklık düzeyinin kalıp içi akışa özellikle de menisküs bölgesine etkisini belirlemek için yapılmıştır. Sonuçlar menisküs hızlarının kayar kapak ile kontrol edilen sistemde açıklık düzeyinden önemli derecede etkilendiğini göstermektedir. Sabit hacimli döküm olarak belirlenen durağan durumdaki operasyonlarda değişik kayar kapak açıklıkları aynı kalıp içi akışı sağlamamaktadır. Fakat durdurucu bar ile kontrol edilen sistemde, durdurucu barın açıklık düzeyinde ki değişimler menisküs hızlarını değiştirmemektedir ve durdurucu barla kontrol edilen sistemlerde açıklık değişikliği kalıp içi akış yapısını etkilememektedir.

Anahtar kelimeler: Kalıp içi akış, Sürekli çelik döküm, Hesaplamalı Akışkanlar Dinamiği, Türbülans modellemesi, Akış kontrolü, Durdurucu bar, Kayar kapı.

To my parents ...

ACKNOWLEDGMENTS

The author wishes to express his deepest gratitude to his supervisor Assoc. Dr. Mehmet Metin Yavuz for his guidance, advice, criticism, encouragements and insight throughout the research.

This thesis would not have been possible without the help and support of my dearest friends and colleagues Mahmut Murat Göçmen, Yiğitcan Güden and Merve Özdemir.

I must also acknowledge the support of the valuable members of Yavuz Research Group, especially: Gökay Günacar and İlhan Öztürk.

I must also recognize the precious friendship of my personal physicians Dr. Elif Haznedaroğlu and Dr. Ezgi Kaya for keeping me healthy during the troublesome thesis study period.

Last but not the least, I would like to thank my beloved immediate family: my parents Nejla and İsmail Gürsoy and my elder sister, Seda Zeynep Gürsoy, for their continuous support throughout my life.

This study was supported by the Middle East Technical University (METU) BAP (Scientific Research Projects) Coordination. Grant No: BAP - 03-02-2012-001.

TABLE OF CONTENTS

ABSTRACT	v
ÖZ.....	vii
ACKNOWLEDGMENTS.....	x
TABLE OF CONTENTS	xii
LIST OF TABLES	xiv
LIST OF FIGURES.....	xv
NOMENCLATURE.....	xviii
CHAPTERS	1
1.INTRODUCTION.....	1
1.1 Continuous Casting Process.....	2
1.2 Flow Measurement in Continuous Casting.....	8
1.3 Modeling of Continuous Casting.....	9
1.4 Motivation of the Study	10
1.5 Aim of the Study.....	11
2. LITERATURE REVIEW.....	23
2.1 Physical Modeling	23
2.2 Previous Work of Physical Modeling	25
2.3 Computational Modeling	28
2.4 Previous Work of Computational Modeling.....	29
3.MODEL DEVELOPMENT	39
3.1 Simulation Domain	39
3.2 The Mesh and Solution Parameters	41

3.3	Turbulence Models	46
3.4	Flow Controller Effect	49
4.	RESULTS AND DISCUSSION	51
4.1	Mesh Independency Study	51
4.2	Turbulence Model Comparison	52
4.3	Influence of Flow Controller	55
5.	CONCLUSIONS.....	71
5.1	Summary and Conclusions	71
5.2	Future Work.....	72
	REFERENCES.....	73
	APPENDIX.....	73
	A-Jet Angle Calculation	83

LIST OF TABLES

TABLES

Table 2. 1 Selected nondimensional groups	24
Table 3. 1 Dimensions and boundary conditions of the model	40
Table 3. 2 Summary of mesh independence study	42
Table 3. 3 Slide gate opening parameters	49
Table 3. 4 Stopper rod opening parameters.....	50
Table 4. 1 Jet angle comparison	62

LIST OF FIGURES

FIGURES

Figure 1.1 A continuous casting machine [34]	12
Figure 1.2 Schematic view of the continuous casting [8]	13
Figure 1.3 A schematic view of tundish, nozzles and the mold [4]	14
Figure 1.4 Schematic representation of different tundish flow controllers [35]	15
Figure 1.5 a) Stopper rods and their cross section, b) illustration of stopper rod opening [36-37]	15
Figure 1.6 Schematic illustration of slide gate openings [10]	16
Figure 1.7 Samples of copper walled molds [38-39]	16
Figure 1.8 Flow within the mold [40]	17
Figure 1.9 Schematic representation of mold flow related problems [41]	18
Figure 1.10 Spray nozzle cooling system for a slab caster [42]	18
Figure 1.11 Oxy-fuel cutting of a continuous casting slab [43]	19
Figure 1.12 Representation of the cross sections of the different continuous casting products [5]	19
Figure 1.13 Samples of semi-finished and finished products [44-45]	20
Figure 1.14 Schematic representation of starter, “dummy”, bar mechanism [5]	20
Figure 1.15 Schematic illustration of different continuous casting techniques [4] ...	21
Figure 1.16 Representation of nail board measurement technique [25]	21
Figure 1.17 Illustration of SVC measurement technique [28]	22
Figure 1.18 Pictures of water model a) without and b) with gas injection [32]	22
Figure 2.1 Illustration of a water model [54]	32
Figure 2.2 Velocity magnitude and predicted flow fields a) at the center plane of the SEN, b) 12 mm away from the center plane of the SEN [50]	33
Figure 2.3 a) Instantaneous velocity vectors; left simulation, right PIV, b) time average velocity vector plot; left simulation, right PIV [50]	33

Figure 2.4 a) Flow pattern and average jet measurement, b) history of U velocity 20 mm below meniscus region [50]	34
Figure 2.5 Velocity vectors on the center plane parallel to the broad face of the mold for two different nozzle designs with and without argon injection [28]	35
Figure 2. 6 Comparison of simulation results of cup bottom nozzle with roof bottom nozzle a) velocity vectors on the center plane parallel to the broad face, b) vorticity contours at the meniscus, c) velocity vectors in the nozzle at the different views [28]	35
Figure 2.7 Effect of gas injection on gas volume fraction across the nozzle bore on wide face center plane (1m/min casting speed) [10].....	36
Figure 2.8 Effect of slide gate opening on vertical pressure distribution [10].....	36
Figure 2.9 Qualitative comparison between experimental and numerical results with an inlet velocity of 1.018m/s a) with 2cm oil layer, b) without oil [61]	37
Figure 2.10 Free surface profile for different water flow rate in. a) 0.5m/s, b) 0.8m/s, c) 1.018m/s, upper row water model, lower row CFD simulations [61].....	38
Figure 2.11 Trajectories of bubbles within the mold [61].....	38
Figure 3. 1 Typical simulation domain and boundary conditions used in CFD models	41
Figure 3.2 Slices of the mesh parallel to the side wall at slide gate, SEN and stopper rod inlet respectively	43
Figure 3.3 Convergence history of a typical simulation with standard k-ε turbulence model.....	44
Figure 3.4 Sample monitor point results at a) meniscus region, b) port exit plane....	45
Figure 4.1 Normalized velocity vectors at the center plane of the mold for two different meshes	58
Figure 4.2 Meniscus velocities at the center plane of the SEN for six different meshes	58
Figure 4.3 Velocity values for six different meshes (a) at the center of the port exit, (b) at 6 mm away from center of the port exit, (c) at 12 mm away from center of the port exit.....	59

Figure 4.4 Normalized velocity vectors at the center plane of the mold for three different turbulence models.....	60
Figure 4.5 Meniscus velocities at the center plane of the SEN for three different turbulence models	60
Figure 4.6 Velocity values for different turbulence models (a) at the center of the port exit, (b) at 6 mm away from center of the port exit, (c) at 12 mm away from center of the port exit	61
Figure 4.7 Average velocity values for three turbulence models and PIV data.....	62
Figure 4.8 Evaluation of different turbulence models by (a) speed of jet along its direction, (b) u velocity values for meniscus region	63
Figure 4.9 Normalized velocity vectors at the center plane of the mold for five different slide gate openings	64
Figure 4.10 Velocity vectors (a) at slide gate region on the symmetry plane, (b) at nozzle region on the symmetry plane, (c) at nozzle region on the port exit plane.....	65
Figure 4.11 Meniscus velocities at the center plane of the SEN for five different slide gate opening	66
Figure 4.12 Normalized velocity vectors at the center plane of the mold for five different stopper rod openings	67
Figure 4.13 Velocity vectors (a) at stopper rod region on the symmetry plane, (b) at nozzle region on the symmetry plane, (c) at nozzle region on the port exit plane.....	68
Figure 4.14 Meniscus velocities at the center plane of the SEN for five different stopper rod openings	69

NOMENCLATURE

f_A	Area fraction of slide gate opening
f_L	Linear fraction of slide gate opening
Fr	Froude Number
H_T	Tundish height (m)
k	Turbulence kinetic energy (m^2/s^2)
L	Vertical distance of stopper rod opening (mm)
R	Radial distance of stopper rod opening (mm)
Re	Reynolds Number
CFD	Computational fluid dynamics
PIV	Particle Image Velocimetry
SEN	Submergence Entry Nozzle
SST	Shear Stress Transport
SVC	Sub-Meniscus Velocity Control
UTN	Upper Tundish Nozzle
ε	Rate of dissipation of turbulence (m^2/s^3)
μ_t	Turbulent viscosity (Pa.s)
ν	Kinematic viscosity (m^2/s)
ω	Rate of specific dissipation of turbulence (s^{-1})

CHAPTER 1

INTRODUCTION

Steel is among the key materials for the world industry and economy. It is utilized in every aspects of live. Steel is a very green product due to its low per ton CO₂ emission rate relative to the other products [1]. Steel has other environment-friendly properties: It is 100% recyclable and has an infinite life cycle. Each year nearly 1,500 million tons of steel are solidified worldwide [2]. Turkey occupies the eight spot in the crude steel production rankings. Casting of steel can be performed by several methods where continuous casting has the domination over others. More than 95% of steel produced in the world are casted by continuous casting [2-3].

Despite all of its commercial success, continuous casting is relatively a new method. Continuous casting was not very popular until late 1960s [4-5]. Ingot casting was the arch casting type with its stationary nature and multistep process. During mid-1800s Henry Bessemer managed to perform the strip casting, which is the pioneer of the modern continuous casting process. The advantages of continuous casting over the ingot casting includes: high productivity rate, better steel quality and more efficiency in terms of labor and energy [6]. This new technology contains several problems due to high surface temperatures, low thermal diffusivity and low casting rates. The worst of the problems however, was the breakouts. Breakout is the case in which solidified steel sticks to the mold and breaks causing molten steel to pour over the machine. 1934 Junghans eliminated the breakouts by oscillating the mold [4, 7].

The process of steelmaking is divided into two main subcategories. The first one is primary steelmaking. Primary steelmaking is responsible for transforming molten pig iron into molten steel with desired metallurgical properties. The solidification of

the molten steel takes place during secondary steelmaking, which follows the primary steelmaking. Continuous casting, also named as strand casting, is a secondary steelmaking technology. In Figure 1.1 a continuous casting machine is demonstrated.

1.1 Continuous Casting Process

Continuous casting starts with a ladle of molten steel. In a ladle metallurgy station, ladles full of molten steel adjusted as desired in chemistry and temperature are prepared [5]. Then the ladle is carried to the casting machine and liquid steel is poured into a smaller reservoir, named as tundish, by a valve system at the bottom of the ladle [8]. In order to preserve the continuity of the process ladles are replaced with the new ones as they run out of the molten steel. Therefore, tundishes must be is large enough to carry necessary molten steel during ladle changes. Tundishes are reinforced with insulation materials in order to withstand the hostile environment arising from the high temperature of molten steel. Nevertheless, tundishes require regular replacements since they have certain operation life. Tundish is also responsible for floating out the inclusion particles into the slag, therefore acts like a refining vessel [9]. These inclusion particles are very dangerous for the final steel quality; they may cause formation of slivers in the final product or may create internal defects and shortens the fatigue life [4-5, 8]. The overall continuous casting process is schematically illustrated in both Figure 1.2 and Figure 1.3.

The molten steel is transferred from the tundish to the mold where the solidification takes place. There are several techniques for controlling the flow rate from the tundish into the mold: Metering nozzles, stopper rods and slide gates. These three flow controller types are shown in Figure 1.4.

The simplest and the cheapest of the of control systems is metering nozzles. Metering nozzles differs from the other two techniques. Metering nozzles supplies constant liquid steel flow rate into the mold, whereas stopper rods and slide gates provide

constant casting speed [5, 9]. This difference creates a disadvantage for the metering nozzles because changes in the casting speed are not preferred in continuous casting. Metering nozzles are generally utilized for the casting of low quality steel since air entrapment to the molten steel, therefore reoxidation, is inevitable [5, 9].

Stopper rods and slide gates are preferable for preventing the air entrapment and making better qualified steel products [5, 9]. Figure 1.5a shows examples of the stopper rods used in the process and Figure 1.5b illustrates stopper rod opening mechanism. They adjust the flow rate into the mold by changing the opening area and they are used with a SEN (Submerged Entry Nozzle) to carry the flow into the mold. Stopper rod, which is a hydraulic system, can be controlled automatically or manually. Controlling the flow rate with stopper rods is trickier than controlling with a slide gate. This comes from the fact that stopper rod is to be driven all the way through the molten steel in the tundish [5, 9]. Moreover, stopper rods require additional regulations for stopping the flow in emergency cases. However, stopper rod has its own advantages over the slide gate systems. Stopper rod offers better protection against air entrapment and provides more uniform distribution of flow in SEN ports [5, 9]. Moreover, stopper rods block molten steel from entering the upper tundish well, and prevent freezing which may occur shortly after the process starts. They also prevent any slag entrapment by blocking the vortex formation above the tundish well [5, 9].

Tundish slide gates are located just below the UTN (Upper Tundish Nozzle), and allow molten steel to enter the SEN. Flow control is achieved by adjusting the overlapped part of the plates, as demonstrated in Figure 1.6 [9, 10]. Steel flow rate through the slide gates are directly related to the molten steel height in tundish and pressure drop through the slide gate. Flow rate is in direct proportion with the tundish height and slide opening. There are two most common approaches to determine the opening fraction of the slide gate [9]. Area fraction f_A , is the ratio of the overlapping area to nozzle bore area, whereas linear fraction f_L , is the ratio of the throttling plate to the bore diameter of the nozzle [9, 10].

Passing through the control systems, molten steel enters to the copper mold. In Figure 1.7 different mold types are illustrated. A casting machine may contain multiple molds or just a single one [9]. Mold flow is the crucial step of continuous casting process since it directly determines the quality of the final product [1]. The important phenomena in mold includes but not limited to: Inclusion removal and transportation, top surface level fluctuations and entrapment of the slag layers, clogging of the SEN, entrapment of gas bubbles [11-13].

The primary cooling of the molten steel starts as it enters the mold. The continuous water cooling from the mold sidewalls removes heat from the steel and solidification starts [5, 8]. Oscillation of the mold takes place in the vertical direction to prevent newly solidified shell from sticking to the mold and causing breakouts. This new solid shell is withdrawn from the mold steadily. Here, a ribbon like body, contains both liquid and solid steel, is generated. This new body is also called as “strand”. Motor driven rolls on the both sides of the strand, which are located below the mold exit and are named as support rolls, provide the motion of the solidified steel through the casting machine [5]. Support rolls helps strand to withstand the heavy ferrostatic pressure. Moreover, support rolls guaranties the withdrawal rate of the strand, which is the casting speed, is equal to the rate of the incoming steel. The overall flow structure within the mold is represented in Figure 1.8. Therefore, continuous casting runs in a steady nature where the liquid level in the mold is kept constant [11, 12].

Mold powder is an oxide-based material used for chemical and thermal insulation. In order to supply protection from the atmosphere mold powder is added to the top surface. Here, molten steel forms a curve shaped “meniscus region” with liquid, solidified mold powder [8, 13]. Meniscus region is the key for a successful steel casting [1]. The initial solidification starts at meniscus where the most important quality problems such as oscillation marks and surface cracks occur. In addition to the aforementioned duties, mold powder also acts as a lubricant. Mold powder melts upon meeting the molten steel being~1500°C, then a portion of the liquid powder leaks into the gap between the mold and the strand [4, 8]. There molten powder acts as a lubricant and prevents sticking. Mold powder also controls the heat transfer at the top of the

mold. Part of the molten powder creates a “rim” near the mold walls which restricts heat transfer. Above the molten steel yet another portion of the molten powder creates a liquid “slag layer”. This liquid slag layer helps removing inclusions such as alumina [8, 13].

Mold flow is the most important part of the casting process as it ultimately defines the final quality of the products. Mold, defined as the heart of the casting, is the last step involving liquid flow hence, the problems occur in the mold cannot be corrected later on Figure [9, 10]. Most of the quality problems on the final product arise from the poor flow control in the mold particularly the meniscus region where the solidification starts [14]. The flow problems that will be presented here are demonstrated in Figure 1.9. Level fluctuations in top region of the mold leads to sudden jumps in the surface which eventually cause molten steel to pour over the machine. Sudden jumps may also create a hook shape extended meniscus which causes slag and bubble entrainment [9, 14]. The captured bubbles creates defects called as “pencil pipes” [14]. Uneven distribution of liquid steel flow the SEN port creates periodic oscillations which eventually also creates slag entrainment [15]. Mold slag can also be trapped in the molten steel due to vortexing and high-velocity flow which causes shearing of the slag from the surface [14]. Jet impingement onto the steel-slag interface associated with a single roll flow pattern, such as induced by excessive gas bubble injection can also cause the slag emulsification [15]. Flow asymmetry within the mold is the general cause of vortexing which drags the slag down into the mold. These surface inclusions will cause line defects called as “slivers” in the final product [9].

Once strand leaves the mold; it is subjected to secondary cooling by spraying water or gas as shown in Figure 1.10. Secondary cooling process also helps cooling of the adjacent equipment. Metallurgical length of the steel takes its place here, which is the distance from the meniscus region to where the strand is completely solidified [5]. Metallurgical length generally ranges from 10 to 40 m. After the steel is fully solidified, the strand is cut off. Cutting off can be taken by gas or plasma torches or in some cases by hot saw and shear, as shown in Figure 1.11 [16, 17].

Injection of argon gas into the molten steel is another significant topic in continuous casting. The primary goal of injection into of the argon is to prevent clogging of the tundish nozzles [18, 19]. Argon gas also backs up the floatation of the solid inclusions by sticking and then carrying them to the top surface. The injection greatly alters the flow field within the mold region, hence excessive work required to investigate its behavior [20]. The injection process introduces new problems along with its benefits. Quality problems such as blisters, pencil pipes are directly related with the presence of argon gas. Argon gas can be injected at several different locations through the holes or pores on the nozzle bore [21]. If the flow is controlled by a stopper rod, then argon is injected through tip hole of the stopper rod. However, when a slide gate system is the choice, argon gas may be inserted up to four different points. Selection of argon as the injection gas bases on two main reasons. First of all, in order to avoid chemical reaction the injected gas must be an inert one and among the noble gases argon is the cheapest [17-19].

Continuous casting allows producing steel at different sizes and different shapes, Figure 1.12 represent the different cross sections of continuous casting products, whereas Figure 1.13 presents common products of the process. These products are also called semi-finished products, or simply as semis, indicating that they need further processing in order to become a finished good [5, 22]. Some of the most common shapes will be introduced here. Billets refer to the products which are square in cross section, and ranges from 100-200 mm in thickness. Billets are rolled into long shaped products such as rails, bars, axles and similar stuff. Billets are casted by the single-piece tube molds. Blooms on the other hand are greater in size than billets and can be in either square or rectangular forms. Blooms can be up to 400x600 mm in cross section. One great difference between billets and blooms is that the blooms are casted into the heavy four-piece plate molds [5, 22]. These molds are generally supported with rigid plates. Slabs are casted with similar molds which are used for blooms. Slabs are large rectangular shaped semis ranging from 50-250 mm in thickness and 05.-2.2 m in width. Slabs semis are then subjected to cold rolling to form sheets or plates. Slab casting is divided into three categories according to the thickness of the final product

[5, 22]. The tiniest of slabs, named as “thin slabs”, change between 50-80 mm, while “intermediate slabs” are about 80-150 mm in thickness. The thickest of them, called “conventional slabs”, ranges between 150-300 mm. Strip casting, which is relatively a new process, produces thin sheets between 1-6 mm in thickness [5, 22].

In order to start casting of the steel a bar is located into mold region [5]. This starter bar is generally called as “dummy bar”. The head of dummy bar, also called as stool, forms a temporary bottom. The top of the stool is reinforced by chill stock materials to help solidification [5]. Dummy bar is slowly withdrawn from the machine when enough steel is solidified within the mold and mold is nearly full. Figure 1.14 demonstrates the working principles of the starter bar mechanism. Once continuous casting is started it may continue as long as several weeks. Process only stops if molten steel is not fetched to the machine [4, 5].

Continuous casting machine can be in different formations. Curved type continuous casting machines are the most popular type for casting of steel. Vertical type casting machines are not preferred for casting of steel [5, 7]. Height of the machine must be raised in a great amount to ensure better productivity requires. Increasing machine height leads to such high ferrostatic pressure that bulging of the strand becomes inevitable [23, 24]. Therefore, vertical casting utilized for casting of lighter metals, such as aluminum, for special applications. Horizontal casting allows shortening of the liquid height, hence overcomes the ferrostatic pressure problem. The issue with the horizontal casting is obtaining a sound initial solidification, and other surface quality problem called as witness marks. Despite its drawbacks horizontal casting is popularly used for casting nonferrous alloys and steel. The newly growing trend, strip casting, is useful for producing thin goods of nonferrous alloys and steel [23, 24]. These four casting formations are demonstrated in Figure 1.15.

1.2 Flow Measurement in Continuous Casting

Continuous casting is a very expensive process which runs in harsh environment. This situation makes the empirical research on the real caster very difficult and limited. The molten metal cripples the submerged probe flow meters with its high temperature, hence measurement techniques such as hot wire anemometer is very limited [25]. The opaque slag layer, on the other hand eliminates most of the flow visualization techniques, and Laser-Doppler velocimetry [26, 27]. Nevertheless, some surface velocity measurement techniques such as nail board, sub-meniscus velocity control (SVC) probe and electromagnetic sensors, are still applicable [1]. Nail boards also allow the measure the liquid level profile and the molten slag thickness [25]. Principles of measurements with nail boards are plain simple as presented in Figure 1.16. A board contains nails along with the aluminum wires, is plugged into the molten slag layer of the mold. Boards generally consisting of one or two rows, where each rows holds up to 15 nails [25]. There, it is kept 3-4s for obtaining a layer of thin solidification, also called skull, over the nails. Nails should not remain too long in the caster since the nearly solidified skull may remelt. Upon removal the shape and height of the skull is measured, this gives insights for the local surface velocity profile and the direction of the flow impingement point. Sub-meniscus velocity control (SVC) is another common indirect measurement technique utilized in continuous casting of steel [28]. SVC works with the principle of torque measurement. Working principle of SVC is given in Figure 1.17. Special reinforced probes are dipped into the mold passing through the slag layer. Drag force acting on the submerged probes creates a torque which can be measured. Knowing the shape and the area of the submerged probe, the drag coefficient, C_D , can be determined hence the only remaining unknown is the velocity. Later the velocity can be calculated from equation of drag force [28]. The details of the all measurement techniques can be found elsewhere [25-28].

1.3 Modeling of Continuous Casting

The previously discussed inabilities of the flow measurement techniques, force the researches to focus mainly on the modeling methods for continuous casting. Continuous casting is studied by both physical and computational models [29, 30]. Before the revolution of the computers bulk of the investigations depend on the physical models [31].

Physical models utilize the opportunity that molten steel and water at room temperature have nearly equal kinematic viscosities. This situation helps reaching the necessary similitude criteria with ease. The transparency of water allows the visualization of the flow, and the cold temperature of the water provides a trouble-free environment for measuring devices [31, 32]. Physical models also enable working with the scaled down geometries. Creating a successful physical model depends on satisfying the necessary similitude criteria. Reynolds number similarity has to be guaranteed as most of the flow physical models. Reynolds number provides modeling of the turbulence and flow momentum with success. The flow in the continuous casting tundish and mold are gravity driven [31]. Therefore, Froude number similarity is also to be satisfied. Reynolds and Froude number similarities should be enough for a prospering physical model of continuous casting unless a two phase flow exists. Mentioned earlier, argon gas may be added to the caster at several different points. If this is the case then the Weber number similarity, which is necessary to model the interface of two fluids, has to be achieved simultaneously with the Froude and Reynolds numbers [29, 31]. Physical models are great tools for governing the flow development within the caster. They also provide insight views for defining problems within the casting machine, help designing new geometries and optimizing the process. Figure 1.18 demonstrates a sample water models with and without gas injection. Detailed info about water models and related previous studies are available in the literature view chapter.

The developing power of the computers shifts the balance of the modeling techniques for the favor of the computational modeling. The powerful Computational Fluid Dynamics (CFD) models are being used increasingly for the modeling of the continuous casting. CFD models are very helpful and accurate for modeling of the complex flow structures of the casting process, especially when the mentioned complexity of the flow becomes too much for water models to handle [31, 33]. Handfuls of mathematical models have been developed for the modeling of the continuous casting. Currently, there are several very successful commercial CFD packages, which can handle the modelling of highly turbulent, challenging and two phased structure of the flow within the caster. Even more CFD codes are created for the specific purposes related to casting issues. Extensive past researches were conducted for the mathematical modeling of the continuous casting. Once again, computer modeling will be discussed in details in the literature view chapter of this thesis.

1.4 Motivation of the Study

The liquid steel flow in continuous casting mold is a substantial research topic since the success of the casting process depends mainly on the flow characteristics in the mold region. Mentioned earlier most of the quality problems, such as slivers, pencil pipes, blisters, are directly linked to the poor flow control within the mold, particularly the meniscus region. Therefore, understanding the dynamics of the flow structure within the mold carries vital importance. Turbulent flow within the mold of a caster makes it very difficult for a modest prediction of the flow characteristics. The aggressive environment of the actual casting machines increases the demand for working with the modeling techniques. In order to gain a further insight to the mold flow issues and be able to overcome the problems that may occur, modeling techniques are utilized. Considering the developing power of computational power; the fast, time efficient and powerful CFD modeling will be the choice among the modeling

techniques. Therefore, in this study CFD models will be used to model complex flow structure within the mold.

1.5 Aim of the Study

Continuous casting is known to be operating most efficiently under the steady state conditions. Transport rate of molten steel from tundish to the caster mold is among the parameters desired to be constant. In continuous casting operation of steel, the flow through tundish to the mold is controlled by different flow rate control systems including stopper rod and slide gate. Ladle change operations in continuous casting machines result in liquid steel level changes in tundishes. During this transient event of production, the flow rate controller opening is increased to reduce the pressure drop across the opening, which helps to keep the mass flow rate constant for the reduced liquid steel level in tundish. In literature there is no complete study focusing on the influence of flow controller opening on mold flow structure. The present study, aims to investigate the effect of different flow controllers on mold flow structure using CFD modeling. In addition, the effect of flow controller opening on meniscus flow is quantified.

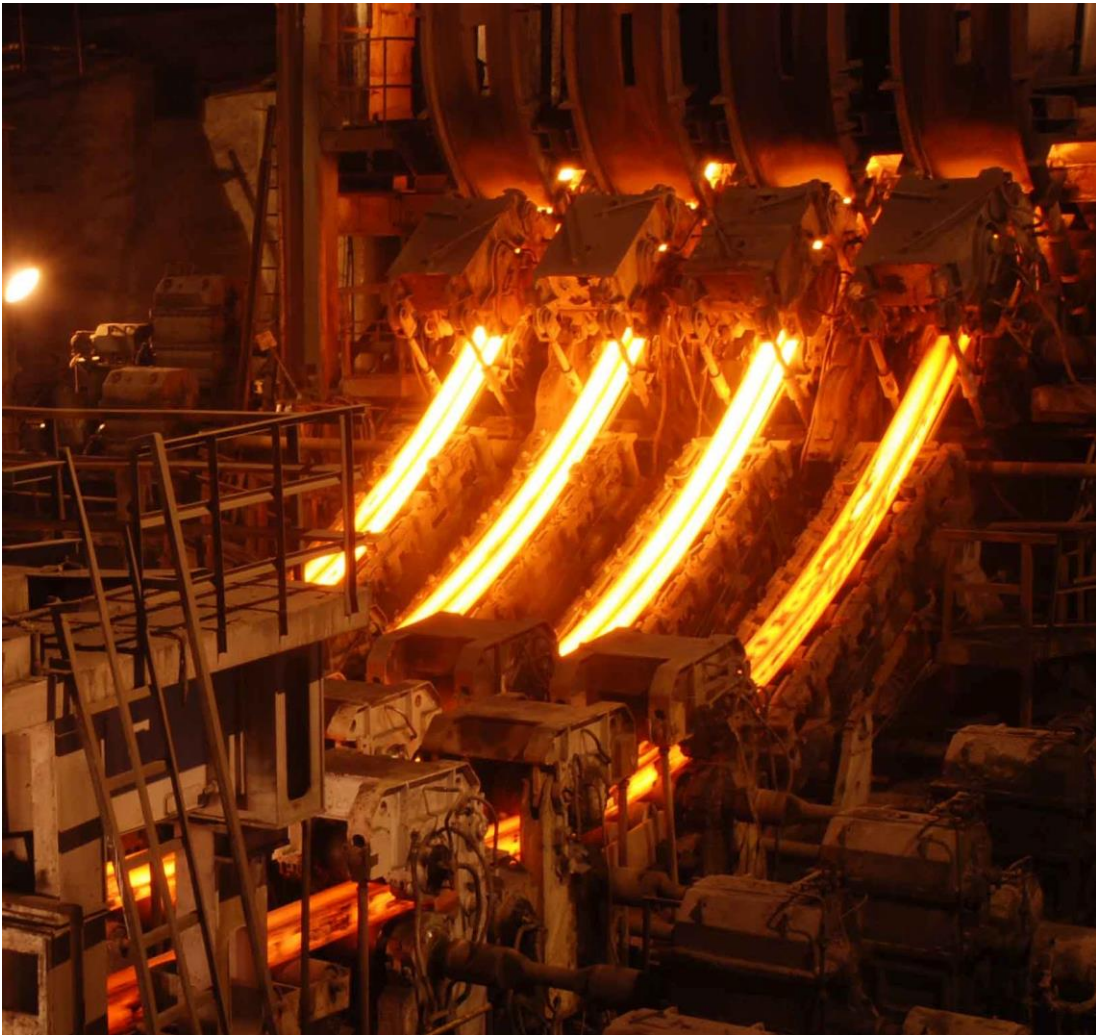


Figure 1.1 A continuous casting machine [34]

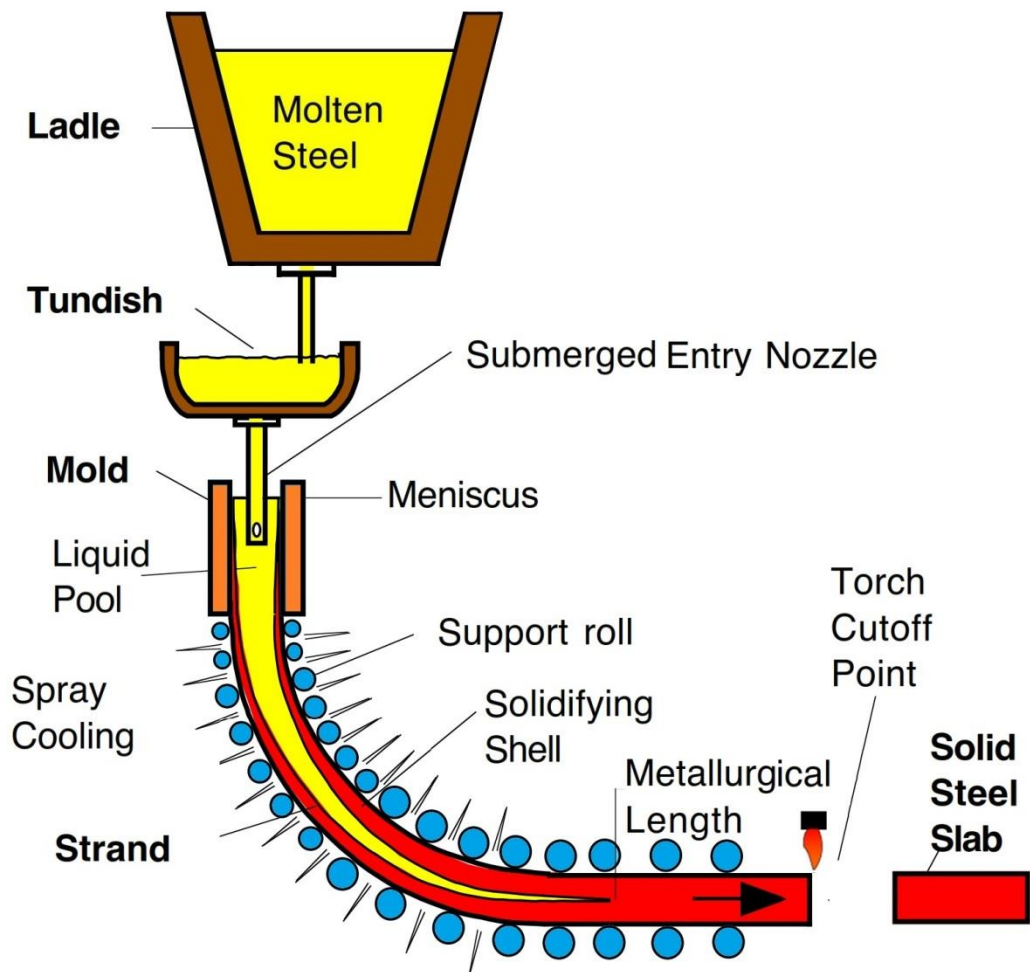


Figure 1.2 Schematic view of the continuous casting [8]

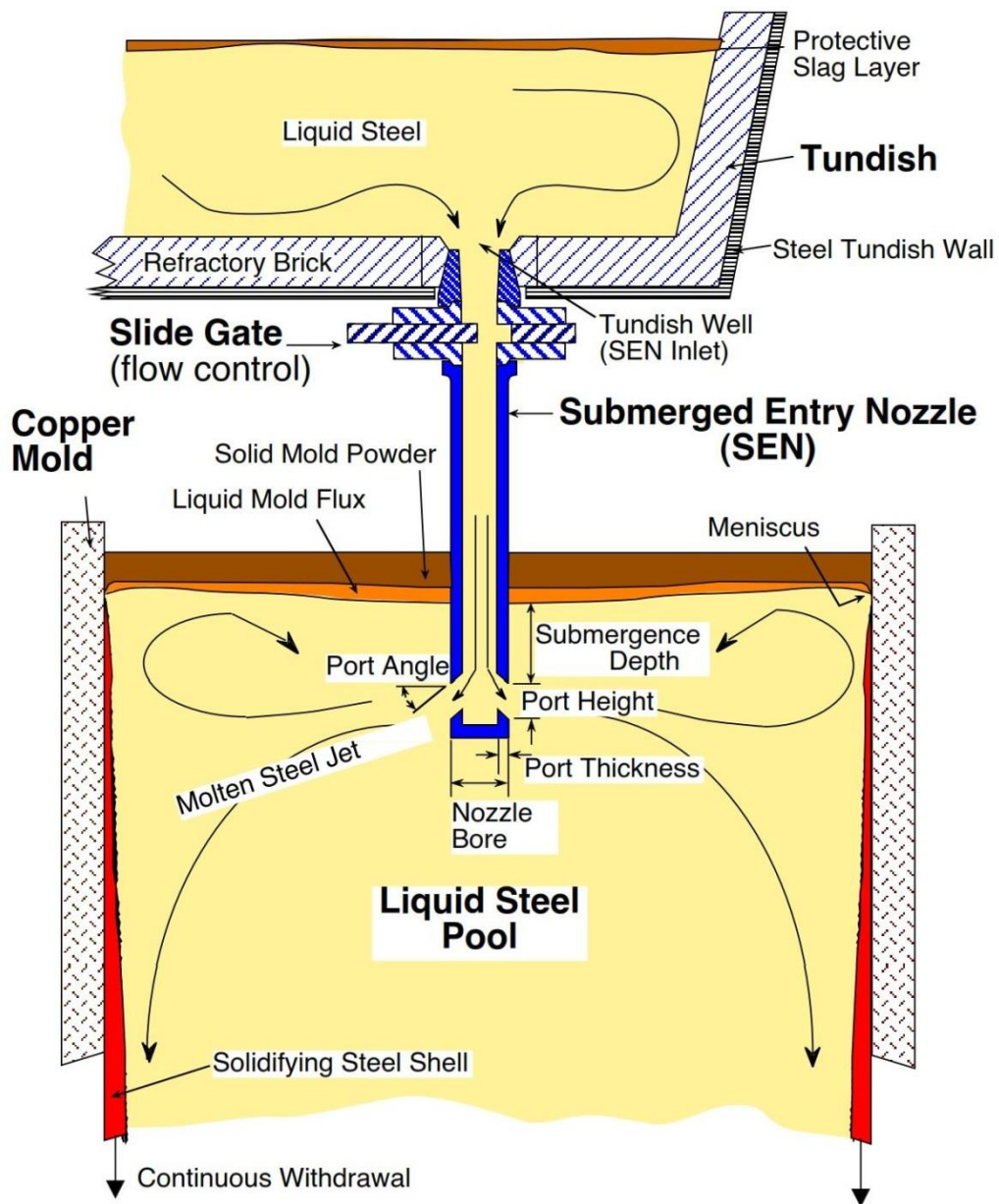


Figure 1.3 A schematic view of tundish, nozzles and the mold [4]

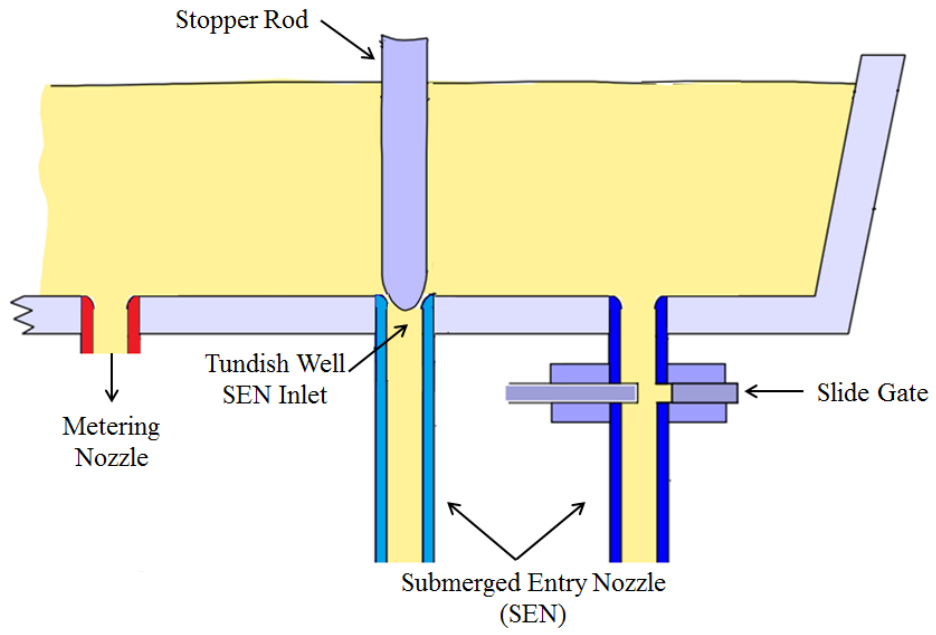


Figure 1.4 Schematic representation of different tundish flow controllers [35]

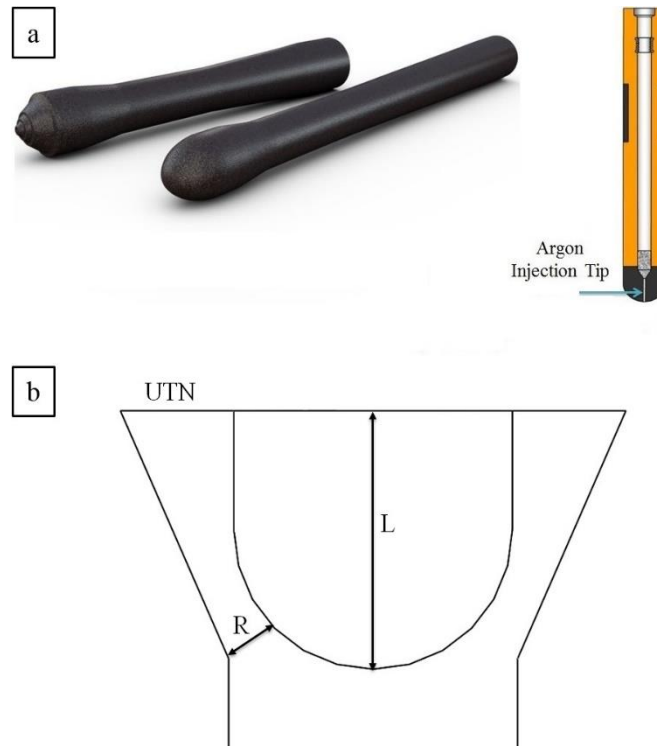


Figure 1.5 a) Stopper rods and their cross section, b) illustration of stopper rod opening [36-37]

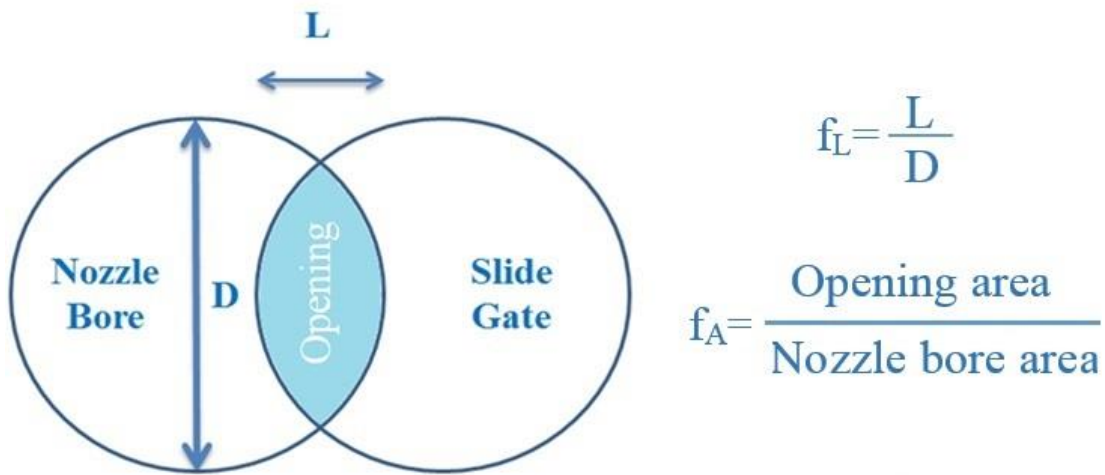


Figure 1.6 Schematic illustration of slide gate openings [10]



Figure 1.7 Samples of copper walled molds [38-39]

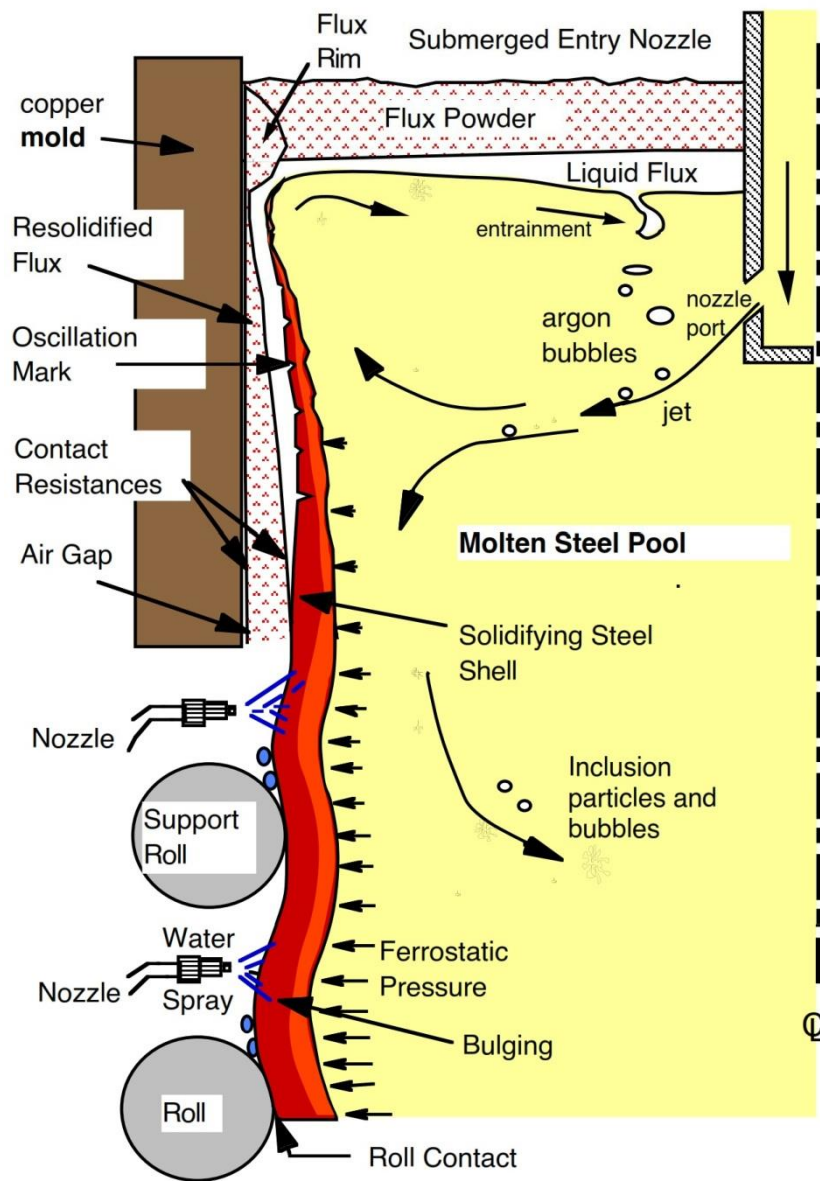


Figure 1.8 Flow within the mold [40]

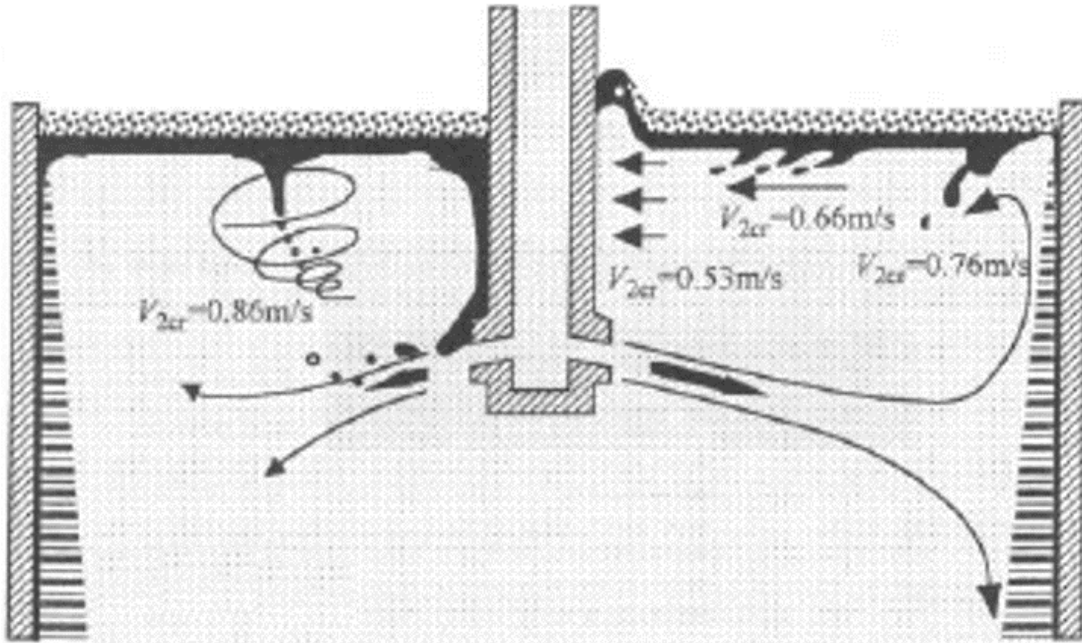


Figure 1.9 Schematic representation of mold flow related problems [41]



Figure 1.10 Spray nozzle cooling system for a slab caster [42]



Figure 1.11 Oxy-fuel cutting of a continuous casting slab [43]

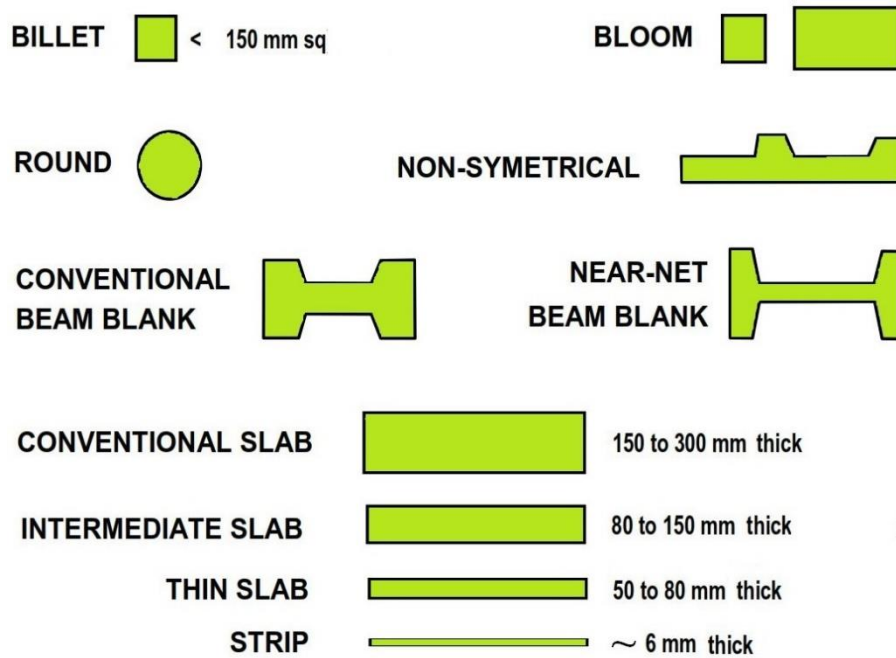


Figure 1.12 Representation of the cross sections of the different continuous casting products [5]



Figure 1.13 Samples of semi-finished and finished products [44-45]

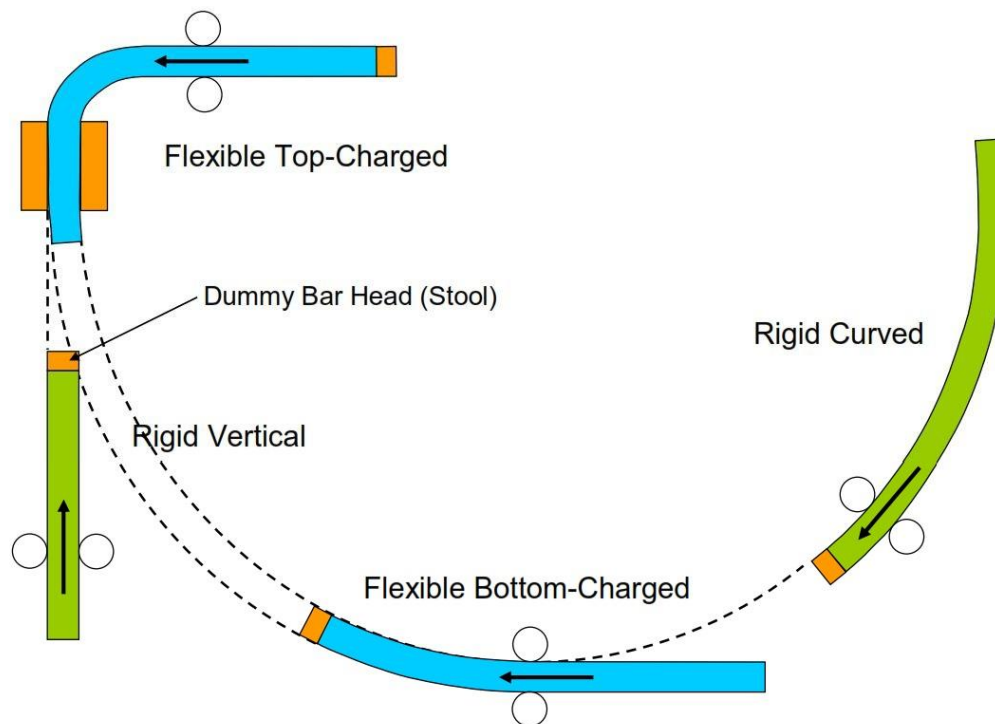


Figure 1.14 Schematic representation of starter, "dummy", bar mechanism [5]

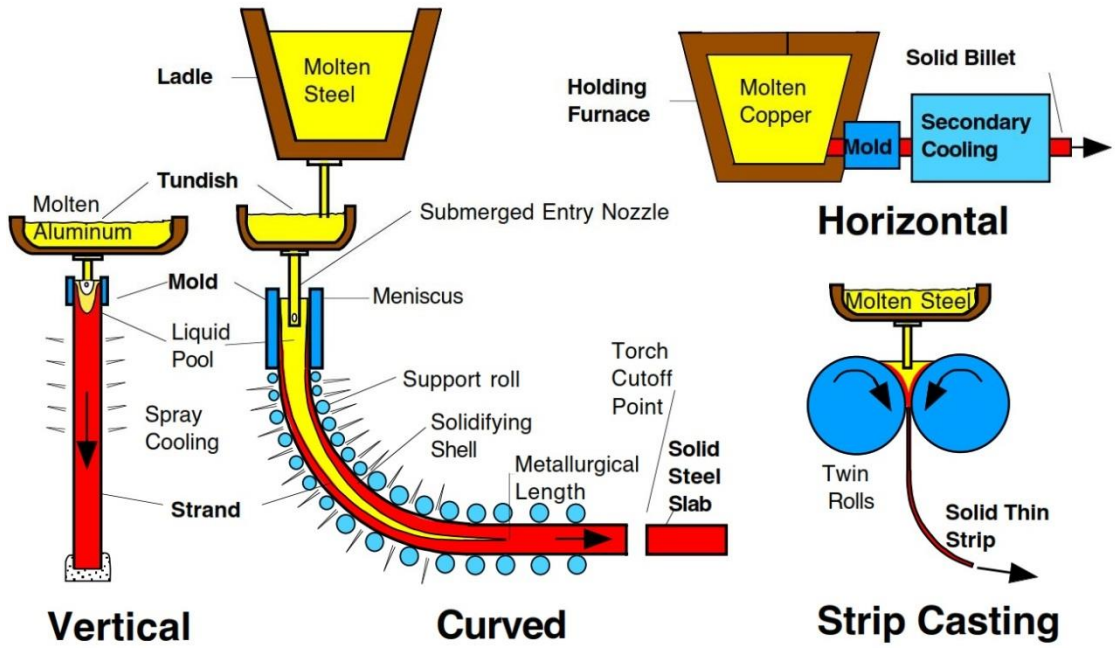


Figure 1.15 Schematic illustration of different continuous casting techniques [4]

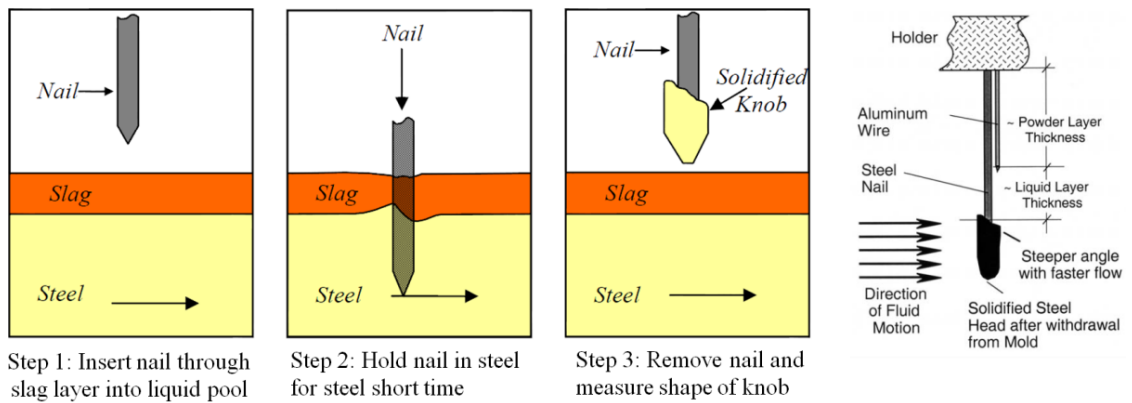


Figure 1.16 Representation of nail board measurement technique [25]

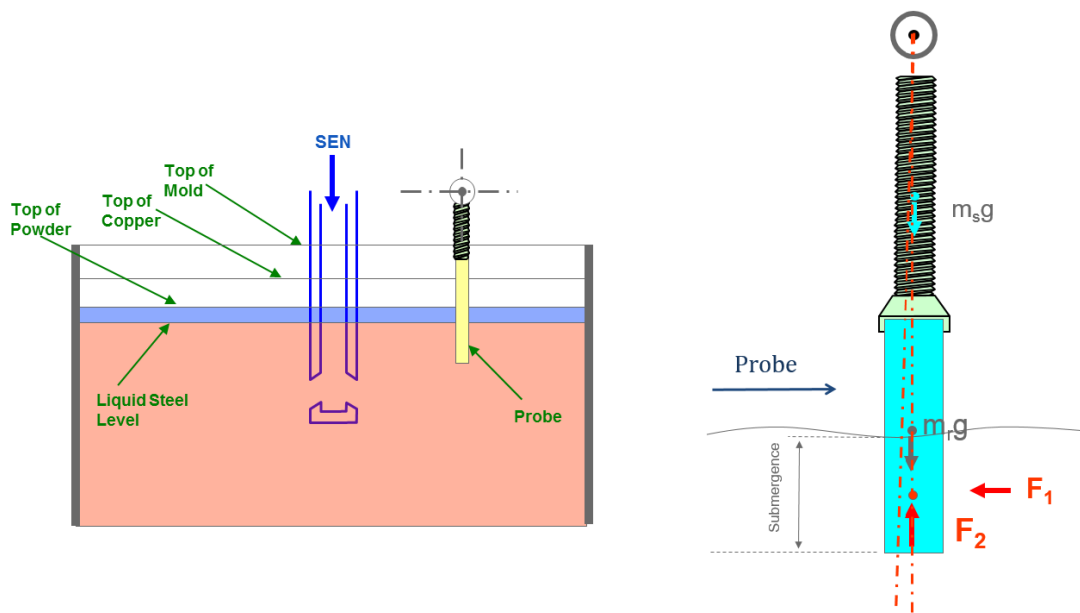


Figure 1.17 Illustration of SVC measurement technique [28]

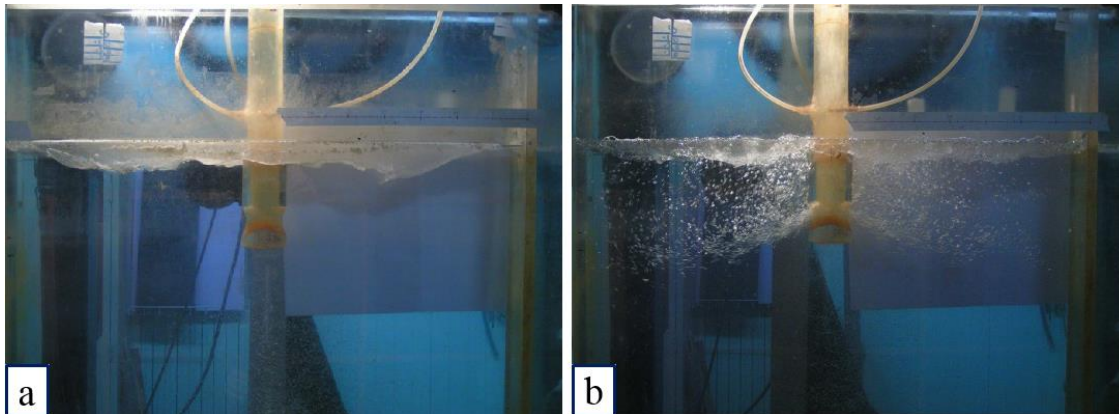


Figure 1.18 Pictures of water model a) without and b) with gas injection [32]

CHAPTER 2

LITERATURE REVIEW

Continuous casting process produces millions of dollars on each and every run, hence the safe going of the process and quality of the products have the utmost importance. Therefore, any work contributing the illumination of the continuous casting process will worth the effort behind. Extensive and elaborate past work were conducted on the different aspects related to the continuous casting issues by both physical and computational modeling. As mentioned in the first chapter, the aggressive environment of the actual casting machines increases the necessity of working with the models. Therefore, the complex turbulent flow phenomena within the casters are studied by the modeling techniques. Modeling of continuous casting is a very helpful application for not only troubleshooting the casting process but also for the testing of the new innovations before their application to the actual casting machines.

2.1 Physical Modeling

The first of the modeling methods that will be introduced is the physical modeling of the continuous casting. Physical models date back to the early days of the wide spreading of the continuous casting process [7, 9]. The physical modeling had had the upper hand over the computational modeling until the rapid development in the power of the computers began. Despite losing the domination to the CFD models, physical models are indispensable, as they provide necessary validation data for computational models [29-31].

Physical models are working with the principle of constructing a successful scale of the actual caster. Laws of a convincing scaling application are demonstrated by the similitude analysis [46]. The three basic laws of similitude, geometric similarity, kinematic similarity and the dynamic similarity, are to be matched between the prototype (actual caster) and the model (physical model) [46, 47]. As indicated by the dynamic similarity the highly dominant force groups in the model must be the identical with those of the model to ensure that the velocity ratios will be same in everywhere [30]. The important force groups are demonstrated by nondimensional groups. The common nondimensional groups used in physical modeling of casting are provided in Table 2.1 [12, 31].

Table 2. 1 Selected nondimensional groups

Dimensionless Number	Ratio of Forces	Formulation	Similarity of Importance
Reynolds Number	Inertia to viscous	$\frac{VL}{\nu}$	Almost All Flows
Froude Number	Inertia to gravitational	$\frac{V}{\sqrt{gL}}$	Gravity Driven Flows
Weber Number	Inertia to surface tension	$\sqrt{\frac{\rho * V^2 * L}{\sigma}}$	Interface Involving Flows
Grashof Number	Buoyancy to viscous	$\frac{g\beta\Delta TV}{\nu^2}$	Natural Convection

The highly turbulent nature of the mold flow makes it required to match the Reynolds number [47]. The same situation also exists for the Froude Number, which is also a necessary similitude criterion due to gravity driven nature of casting process. Water at

295 K (22 °C) has the kinematic viscosity of $0.96 \cdot 10^{-6} \text{ m}^2/\text{s}$, which is very close to the kinematic viscosity of steel $0.81 \cdot 10^{-6} \text{ m}^2/\text{s}$, at 1823 K (1550 °C) [48, 49]. In order to match the Froude and Reynolds Number similarities simultaneously the small difference between the kinematic viscosities of water and steel is neglected and the kinematic viscosities considered to be the same. Then, the only possibility of obtaining a successful similarity of these two nondimensional group numbers is to utilize a full-scale model. However, those two numbers similarities are sufficient as long as the flow is single-phase. When more than one phase is introduced, particularly for modeling of the argon gas injection by air, the Weber Number similarity should also be matched along with Reynolds and Froude Number similarities. If the heat transfer phenomena are also to be studied Grashof number should be matched simultaneously with the other nondimensional groups [46-49]. The physical models has its own limitations. Particularly, when more than one phase is considered, for instance gas injection or top meniscus region, the similarity concept becomes very complex and three different dimensionless criteria have to be satisfied [1, 31]. Froude, Weber and Reynolds numbers have to be kept similar for the prototype and the model for having some meaningful results that can be comparable [1]. The impossibility of achieving these criteria in water models limits the accuracy of experimental modeling with to single-phase flow modeling [1].

2.2 Previous Work of Physical Modeling

Thomas et al. worked on a 0.4-scale Plexiglas water model of tundish, tundish nozzle and the mold of an actual caster, with a slide gate system as flow controller. Flow field is single-phase with no gas is introduced [11]. A PIV system is utilized in order to obtain experimental data. In another research of the same group, the turbulent nature of the single-phase flow was examined [50]. Yet another research of that group focused on a multi-phase flow field. While the other parameters are kept constant the only exception is that air is introduced to the UTN for representing the argon injection [51].

Similar study by Bai H. and Thomas B.G. concentrated on the effect of the gas injection on the highly turbulent flow field of the mold with their 0.4-scale water model [52]. In all these studies they encounter the double roll flow pattern, which was first proved by Szekely et al [53]. They utilize the experimental model results as a validation for the developed CFD models. An illustration of their water model set up is presented in Figure 2.1 [54].

Yavuz et al. worked with full scale water model of a thin slab caster where a PIV system was introduced to collect data [55, 56]. Two different industrial slab caster's molds and SENs were constructed from Plexiglas in full scale to gain knowledge of the flow field inside the caster. The tested SEN designs were four-port and a two-port type; the flow field was single-phase where the solidification effect was neglected. The results of the study indicate that water model is sufficient enough to understand the overall flow structure in the mold. The scale and the location of critical flow structures seen in the water model roughly matches with the ones in the caster [55, 56].

Thomas et al. utilized two different, stopper rod controlled water models to investigate the flow field [57]. The first model had bifurcated types nozzle ports whereas the second one had the trifurcated types. In the experiments both PIV and hot-wire anemometry techniques were used. The second part of the research contains experiments with the same two water models [58]. The purpose was to model the particle movement within the mold region. The modeling was accomplished by using plastic particles to represent the inclusion particles of an actual caster. The results of the study demonstrate that water models are good enough to mimic flow field within the caster [57, 58]. In another stopper rod controlled geometry, Zhang et al. examined a handful of topics [15]. The study contains two different cross sectioned water models. Nitrogen was used to model the argon injection, and control of flow to the mold was provided by a stopper rod. The purpose of the study is to examine the changes in surface fluctuations due to other casting parameters such as SEN submergence depth, casting speed and nitrogen flow rate, SEN inner diameter, nozzle port angles, lower roll's impingement point and pressure (an important parameter for solidification), and also the area ratio, which is the SEN bore area divided by total

nozzle port exit areas. They investigated that SEN flow depends on the flow rates of liquid and gas and the liquid height in the tundish. They also suggest that the gas flow rate should be adjusted with changes in the casting speed in order to maintain stable bubbly flow [15].

Domgin J.F., Gardin P., created a half scale Plexiglas water model of the mold and nozzle [59]. The experimentation set up consists of both LDA and PIV systems where the first one was used taking data at specific points and the second one helped acquiring instantaneous flow field. The multi-phase flow field within the mold is investigated by adding air to flow domain. The overall flow fields and the meniscus velocities presents a good match with their developed computational models [59].

Pericleous et al. published two papers where they constructed a water model on which experimentation were conducted by using LDA measurements [32, 60]. The flow field is multi-phase due to the injection of air and also the presence silicon oil which is inserted to the mold for representing the slag layer on top of the steel. The aim was to gain insights to the steel-slag interface behavior at different flow rates and oil layer thicknesses. They encountered high surface fluctuations as the oil is added to the system [32, 60]. Similar research to that of Pericleous et al. was completed in the thesis of Kountouriotis Z., where the behavior of the slag over the steel was investigated by water-oil model [61]. Effect of the gas injection on the meniscus region also existed within the study. Gas injection tends to reduce the standard deviation of the horizontal velocity component and affects the upper loop from the SEN to the narrow faces. Visualization of numerical results and experimental videos illustrate that the gas affects the upper loop from the SEN to the narrow face [59]. Gupta and Lahiri have also worked on the modeling steel-slag interface [62]. In that study the flow rate and the model are kept constant and different oil-water mixtures were tried [62].

The effect on SEN designs were studied by several researches. Evans et al. investigated various SEN port shapes with the help of a PIV set-up [63]. Meratian M. and Hadjari A. used a full scale water model with a four-hole exit SEN [28]. Different casting speeds and different submergence depths were also examined. The multi-phase flow

field was created by injecting argon gas itself [28]. Gutierrez-Montiel et al. compared two different SEN design on the water model by using both PIV and ultrasonic measurements on the meniscus region [64]. In a full scale water model study by Calderon-Ramos et al. study the effect of misaligned nozzles on the flow field. Improving the flow visualization was provided by dye injection and cameras recorded the flow field [65].

2.3 Computational Modeling

Computational techniques are another powerful tool for modeling the continuous casting process. The fact that the power of the computers are growing stronger and commercial codes computing more accurate than ever, increases the demand for computational modeling of continuous casting process [1]. The difficulty of matching the Reynolds, Froude, Weber and Grashof Numbers simultaneously makes it even more tempting to focus on the computational modeling. However, all the computational models need to be validated against a physical model or actual flow measurements in order to test its reliability and accuracy [31].

Computational modeling is widely used for the different and tricky issues of the continuous casting process. Computational techniques are known to handle variety of the topics related to the casting, those include, but not limited to the: the flow behavior within the caster which is highly turbulent, the heat transfer phenomena between solid and liquid phases, motion of the injected gas through the mold, multi-phase flow structure due to injection argon gas and steel-slag interface, solidification and following shrinkage of steel, transport of heat through the caster, free surface fluctuations, crack formations, transport of the inclusion particles, motion of the mold powder through the gap between solidified shell and the mold walls, the influence of the electromagnetic brake [31].

2.4 Previous Work of Computational Modeling

Thomas et al. worked on the 0.4-scale, slide gate controlled geometry of the nozzle and the mold with the purpose of gaining insights to the overall transient flow field [11]. Utilizing the symmetry conditions, only the half of the geometry was simulated. The single-phase flow field was solved using both LES (Large Eddy Simulation) and k- ϵ turbulence model, which is a RANS (Reynolds-Averaged Navier–Stokes) approach. Figure 2.2 illustrates both flow field within the nozzle and the comparison of velocity magnitudes at nozzle center plane and 12 mm away from the nozzle center plane [11, 50]. According to Figure 2.2 a satisfactory match between the PIV measurement and CFD modeling for nozzle plane velocity magnitudes exists. Figure 2.3 presents the overall flow structure comparison within the mold for both instantaneous and time averaged vector fields. The double roll flow pattern is achieved for both experimental and numerical models. Figure 2.4a demonstrates the mold section of the PIV experiment along the calculated overall jet angle. The experimental jet angle, 29°, is close to the predicted jet angle from the CFD model which is 27.8°. Figure 2.4b presents the meniscus velocity comparison between the models, and once again the measured and predicted values seem to match [11, 50]. In a very similar research of the same group the gas injection was also modeled with the same turbulence models mentioned above, and the findings of the analyses were compared to the physical modeling results [50]. The influence of gas injection was also studied by Wang [66], Cross et al. [67] and Creech [68].

Yavuz M.M. compared two different tundish designs using RANS k- ϵ turbulence model, where the flow field was single-phase and heat transfer was taken into account [28]. The study also contains comparison of different nozzle bottom shapes and different port angles with and without gas injection. The mold flow simulations were conducted using URANS k- ϵ turbulence model [28]. Figure 2.5 presents the velocity vectors on the center for two port up and port down nozzle designs, with and without argon injection. Figure 2.5 shows that the double roll flow pattern exist for both SEN designs when no gas is present. However, port down nozzle designs generates higher

meniscus velocities. The presence of argon gas significantly affects the flow pattern as it clearly damps the upper recirculation zones. Argon gas creates multiple recirculation zones in the meniscus region [28]. Figure 2.6 represents the influence of nozzle bottom designs, roof and cup bottom, on mold flow structure. Despite the fact that both nozzles types produce the classical double roll flow pattern in the mold, the flow characteristics are quite different since jet expansion in the mold (indicated as an arrow) is significantly wider with the roof bottom nozzle. The figure also proves the effect of sliding gate on the flow structure is clearly observed as the quite strong circulation at the bottom of the nozzle is evident and circular jet exits the port. For vortex formations, traditional high levels of vorticity around SEN patterns exist for the cup bottom. On the other hand, roof bottom type produce unorthodox results as the high levels of vorticity appear near the side walls [28]. Similar studies about effect of nozzle design were studied by Thomas et al. [51] and Hershey [69].

Bai H. and Thomas B.G. worked on their slide gate controlled geometry [10, 52]. The flow within the domain was multi-phase with the presence of argon gas. The analyses were conducted using multifluid Eulerian multiphase model built in CFX, later the results were verified using experimentation data and then they investigated the influence of a handful casting parameters such as argon injection rate, gas diameter, slide gate opening fraction, slide gate orientation, casting speed, nozzle port shapes and angles [10, 52]. Figure 2.7 represents the behavior of argon gas concentration at different locations for a specified casting speed. Figure 2.7a demonstrates volume fraction profiles across the nozzle on the wide face center plane at three different locations. Results indicate that the domination of liquid and gas phases in the central region and the near wall regions respectively. Figure 2.7b clearly proves the influence of slide gate opening as the location of high gas concentration shifts towards the newly created swirl zone. However, down in the nozzle flow gets symmetrical as indicated in Figure 2.7c. Mentioned earlier during the ladle changes, the flow rate controller opening is increased to reduce the pressure drop across the flow rate controller opening. The adverse relation between the tundish height, H_T , and slide gate opening is demonstrated in Figure 2.8 for a specific flow rate [10, 52]. Similar studies were

conducted by Liu et al. [70] and Yu et al. [71] and Tsuge [72] where the effects of several casting parameters on mold flow were observed.

Kountouriotis Z., simulated the behavior of the slag over the steel and compared it to the result of the experimental water-oil model [61]. Effect of the gas injection on the meniscus region was also investigated. Figure 2.9a present a good match between the experimental and numerical results of water-oil interface. Air-water interface is also demonstrated in Figure 2.9b and once again there is a good match between the results. One important conclusion from Figure 2.9 is that air-water model produces almost flat interface whereas, for water-oil interface is disturbed [61]. In order to observe the effect on steel flow rate on steel-slag interface, different flow rates were tested. In Figure 2.10 three different flow rates with inlet velocities of 0.5, 0.8, 1.018 m/s were tested. The water model and numerical results are given in the upper and lower rows respectively. Both models clearly indicate that as flow rate increases the disturbance in the oil layer also increases. Finally bubble behavior was investigated as argon gas is introduced to the flow field. In Figure 2.11 the trajectories of bubbles with diameters ranging from 1 to 6.8 mm are demonstrated with lighter grey lines whereas, the trajectories of bubbles with a diameter of less than 1 mm are shown with darker grey lines. Figure 2.11 shows that the larger bubbles tend to move upwards where they escape whereas, the smaller bubbles move downwards into the mold [61]. The interface of slag-steel behavior was also studied by Lei et al. [49], Theodorakakos and Bergeles [74], Pericleous et al. [32] and Panaras et al. [84].

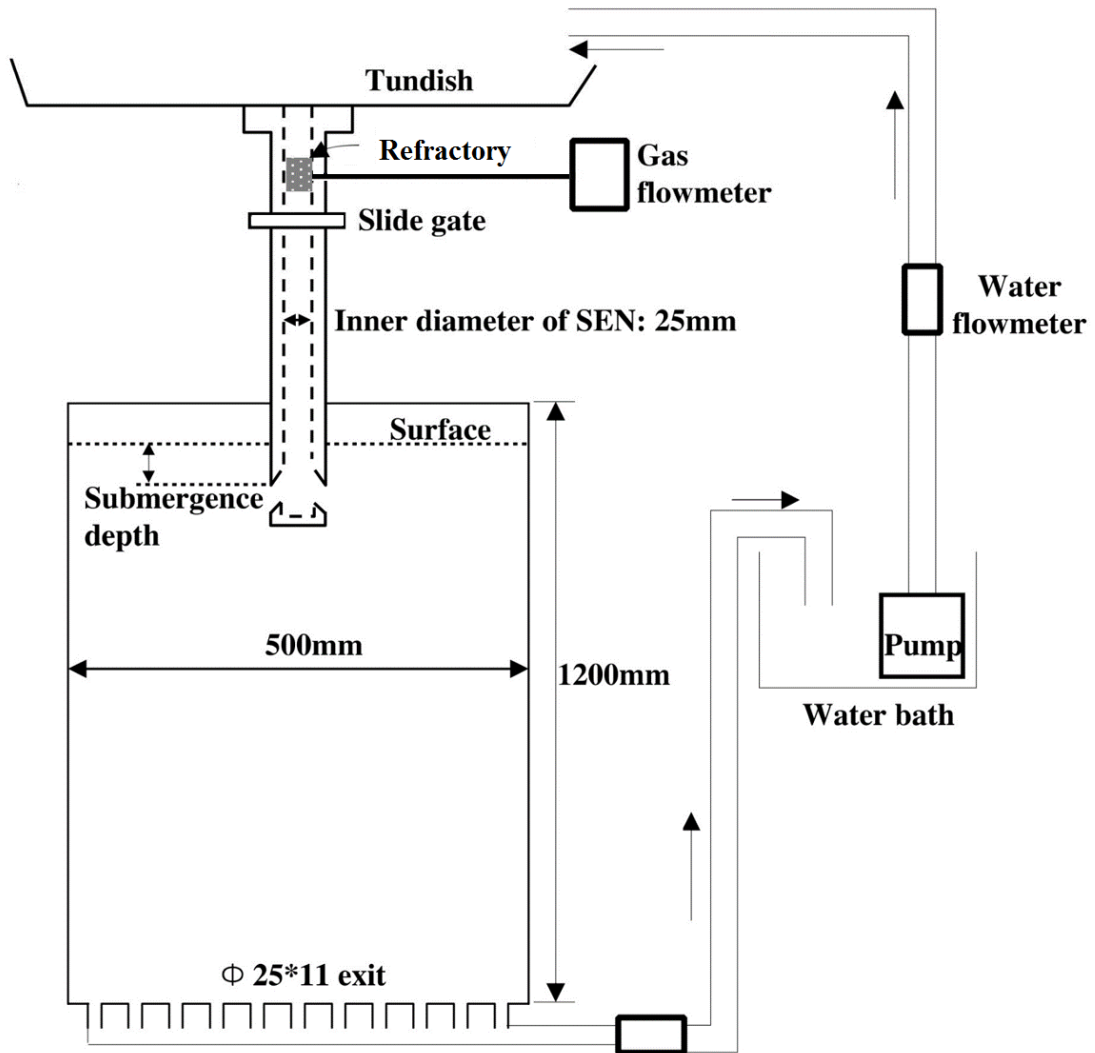


Figure 2.1 Illustration of a water model [54]

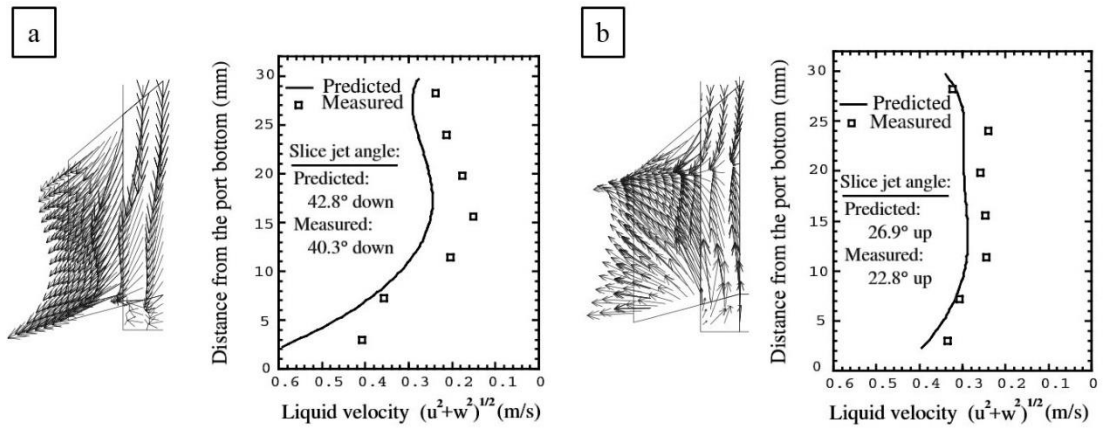


Figure 2.2 Velocity magnitude and predicted flow fields a) at the center plane of the SEN, b) 12 mm away from the center plane of the SEN [50]

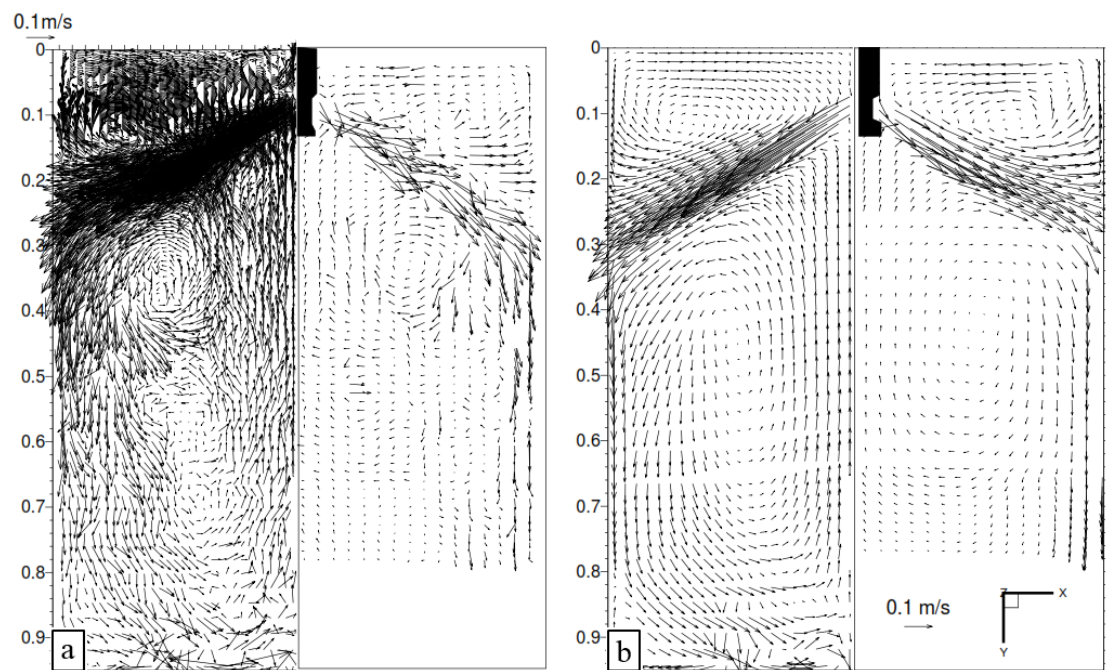
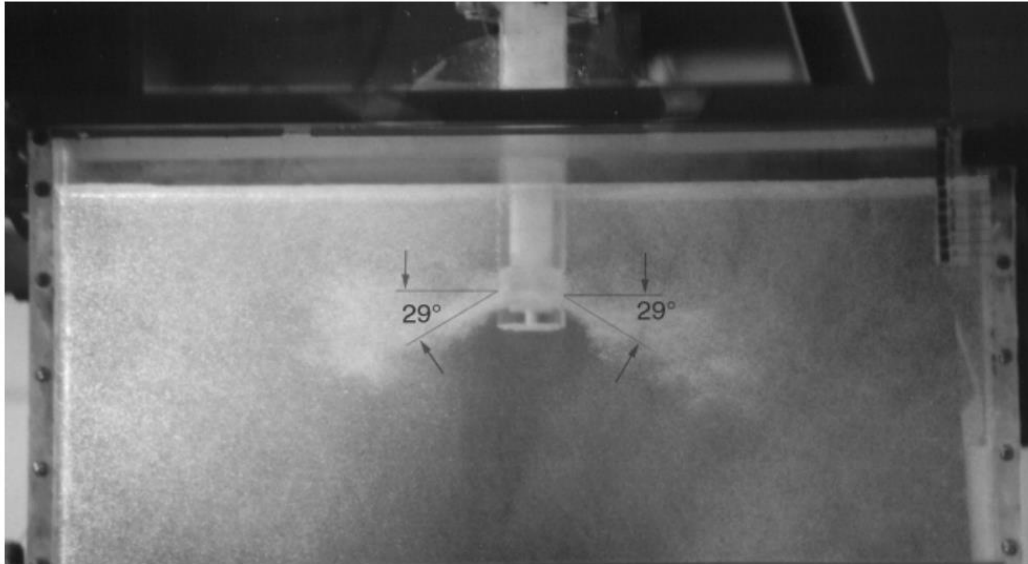


Figure 2.3 a) Instantaneous velocity vectors; left simulation, right PIV, b) time average velocity vector plot; left simulation, right PIV [50]

a



b

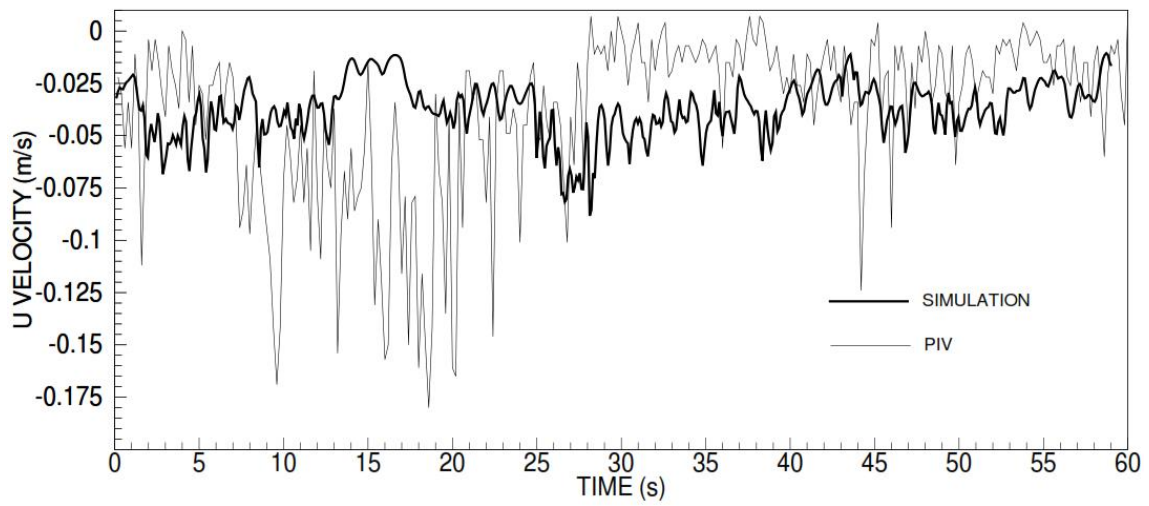


Figure 2.4 a) Flow pattern and average jet measurement, b) history of U velocity 20 mm below meniscus region [50]

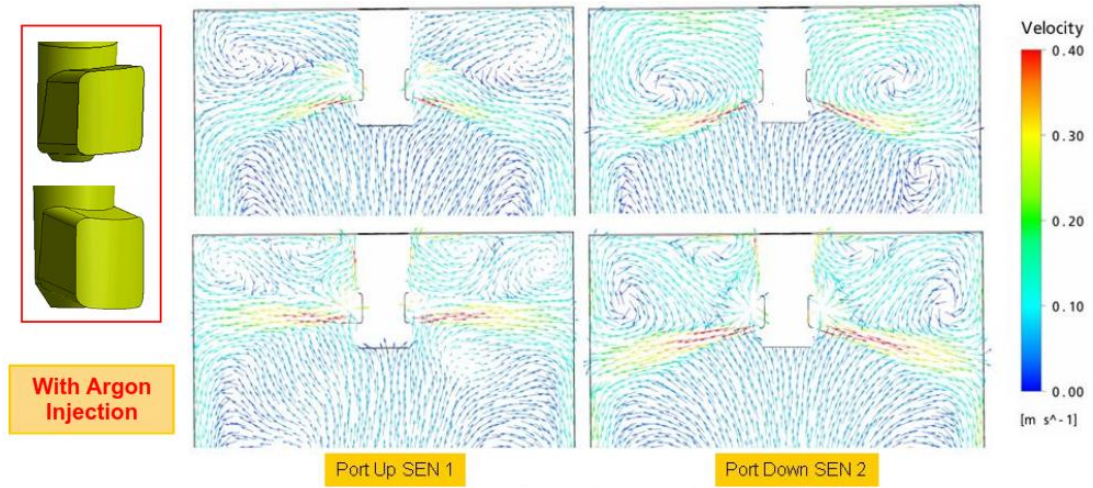


Figure 2.5 Velocity vectors on the center plane parallel to the broad face of the mold for two different nozzle designs with and without argon injection [28]

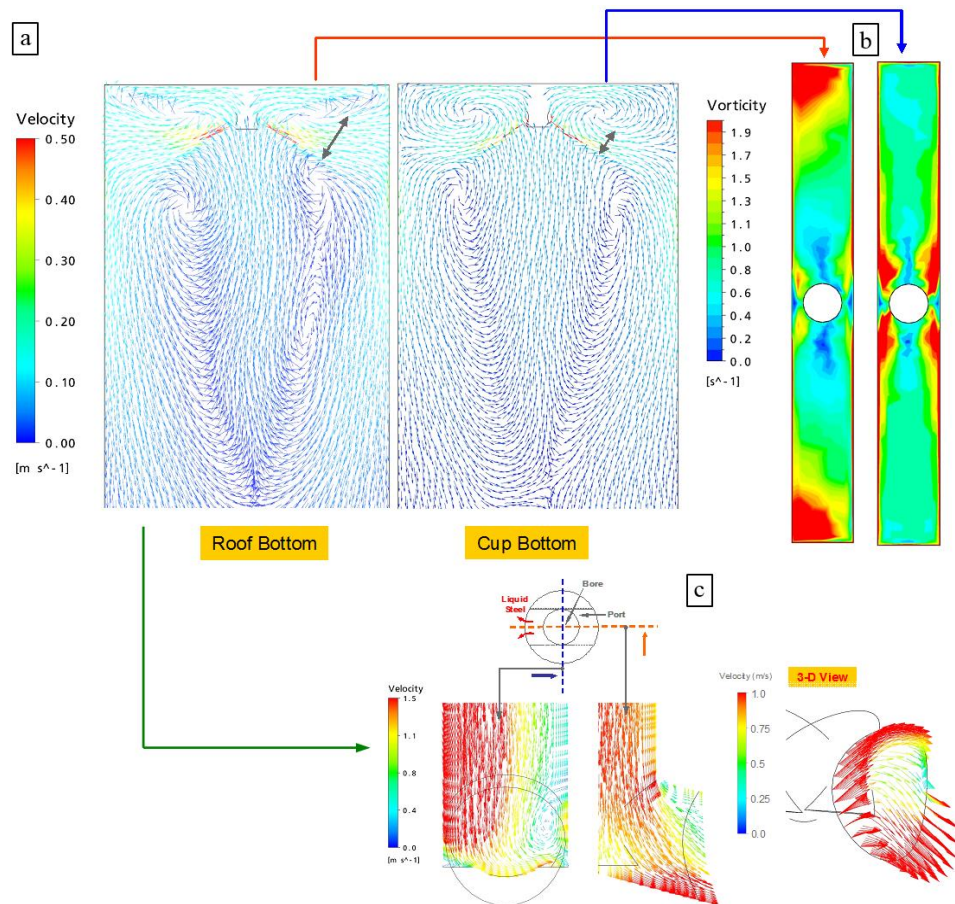


Figure 2. 6 Comparison of simulation results of cup bottom nozzle with roof bottom nozzle a) velocity vectors on the center plane parallel to the broad face, b) vorticity contours at the meniscus, c) velocity vectors in the nozzle at the different views [28]

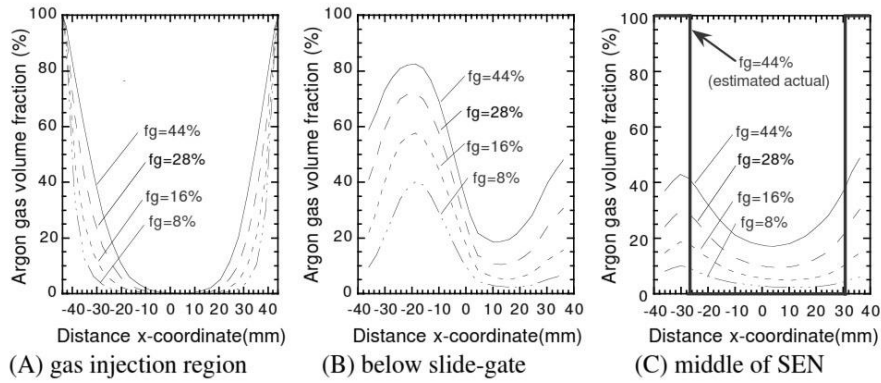


Figure 2.7 Effect of gas injection on gas volume fraction across the nozzle bore on wide face center plane (1m/min casting speed) [10]

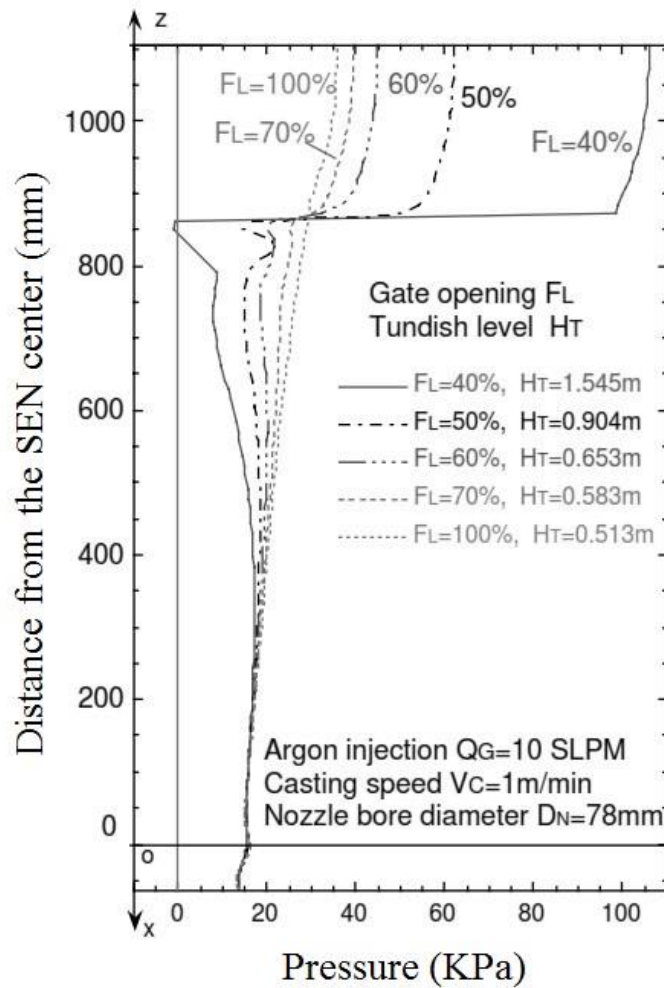


Figure 2.8 Effect of slide gate opening on vertical pressure distribution [10]

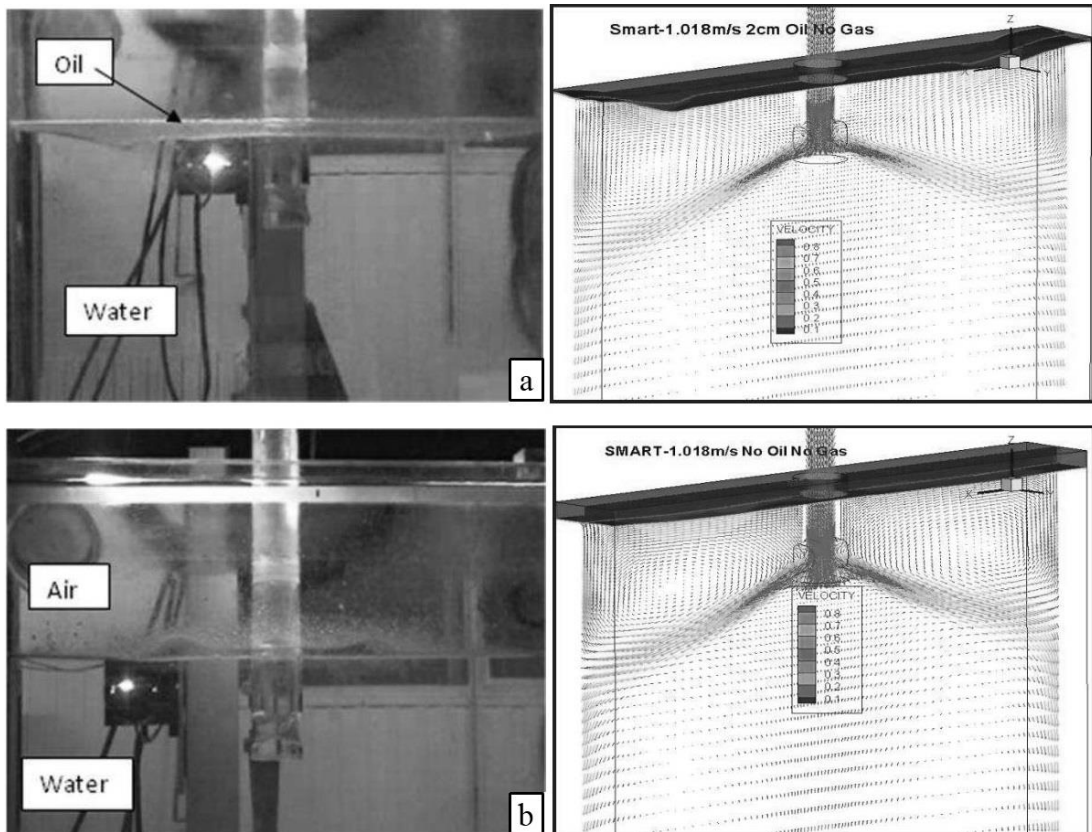


Figure 2.9 Qualitative comparison between experimental and numerical results with an inlet velocity of 1.018m/s a) with 2cm oil layer, b) without oil [61]

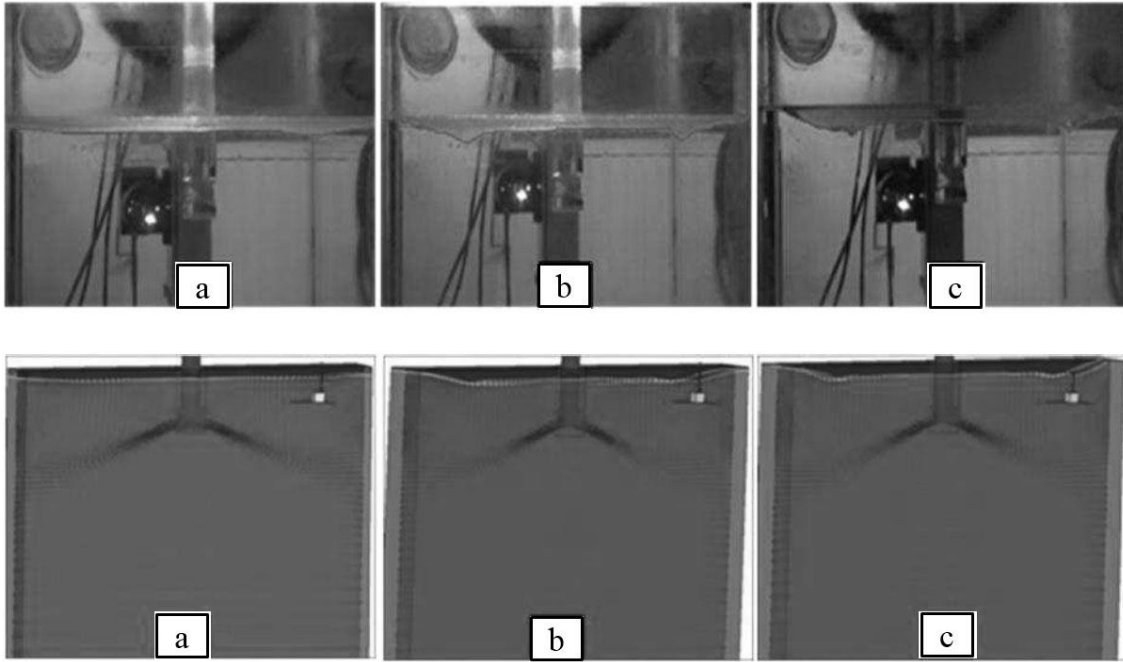


Figure 2.10 Free surface profile for different water flow rate in. a) 0.5m/s, b) 0.8m/s, c) 1.018m/s, upper row water model, lower row CFD simulations [61]

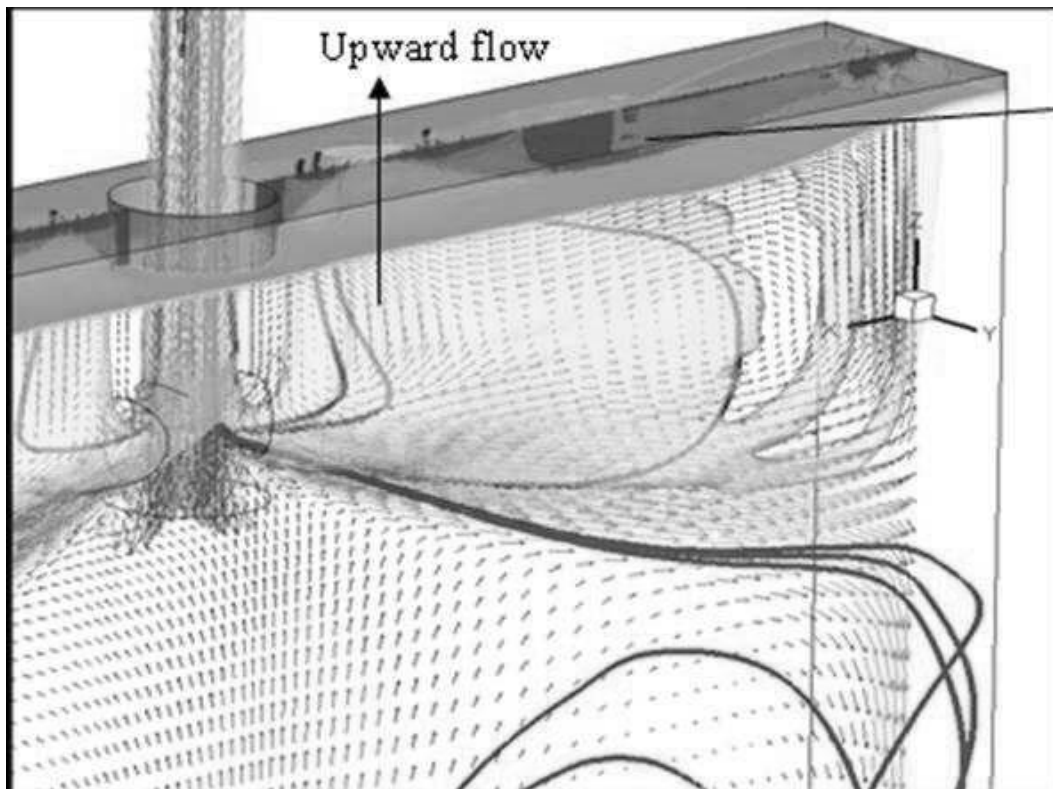


Figure 2.11 Trajectories of bubbles within the mold [61]

CHAPTER 3

MODEL DEVELOPMENT

In this chapter, CFD model development is explained in detail. The model was steady state and developed for single-phase condition where no gas was introduced. The geometry was generated using ANSYS Design Modeler. ANSYS Meshing was used for grid generation. FLUENT was utilized for performing the flow simulations in the present study.

3.1 Simulation Domain

The CFD model was developed for 0.4-scale water model which includes the nozzle and the mold as shown in Figure 3.1 [11, 50]. The particular geometry was selected since the geometry contains sufficient experimental data which was used to validate the CFD model developed in the present study [11, 50]. The details of the geometry along with the corresponding boundary conditions are tabulated in Table 3.1. The thickness of the mold simulation domain was kept constant therefore the reduction in liquid steel domain due to solidification was neglected. Flow control was provided by a slide gate mechanism. The fixed flow rate was supplied from the inlet of the UTN (Upper Tundish Nozzle). Three 35 mm square openings at the bottom surface were the outlet ports. The top surface, meniscus region, was modeled as free slip boundary condition where the flow was free of any shear stresses to simulate the condition for water model test set-up. The side walls including SEN walls were modeled as no slip boundary condition where the fluid had zero velocity relative to the adjacent walls. When the only half of the domain was simulated, the symmetry boundary condition

was utilized. The image on the left of Figure 3.1 demonstrates the simulation domain along with the corresponding boundary conditions for half domain simulations. The images on the right side of the Figure 3.1 demonstrate the zoomed in representation for the slide gate section in the simulation domain along with the stopper rod section that is used in further sections where the effect of different types of flow rate controllers on mold flow is investigated.

Table 3. 1 Dimensions and boundary conditions of the model

Flow rate	0.70 kg/s	Liquid Density	998.2 kg/m ³
Total nozzle length	510 mm	SEN submergence depth	80 mm
Slide gate opening, f_A	40%	Slide gate orientation	90°
Slide gate thickness	18 mm	Slide gate diameter	28 mm
Nozzle bore diameter	32 mm	UTN diameter	28 mm
Port opening	31x31 mm	Port thickness	11 mm
Port upper angle	40°	Port lower angle	15°
Mold length	956 mm	Mold thickness	80 mm
Side walls	No slip	Top surface	Free slip
Inlet	Mass flow rate	Outlet	Pressure outlet

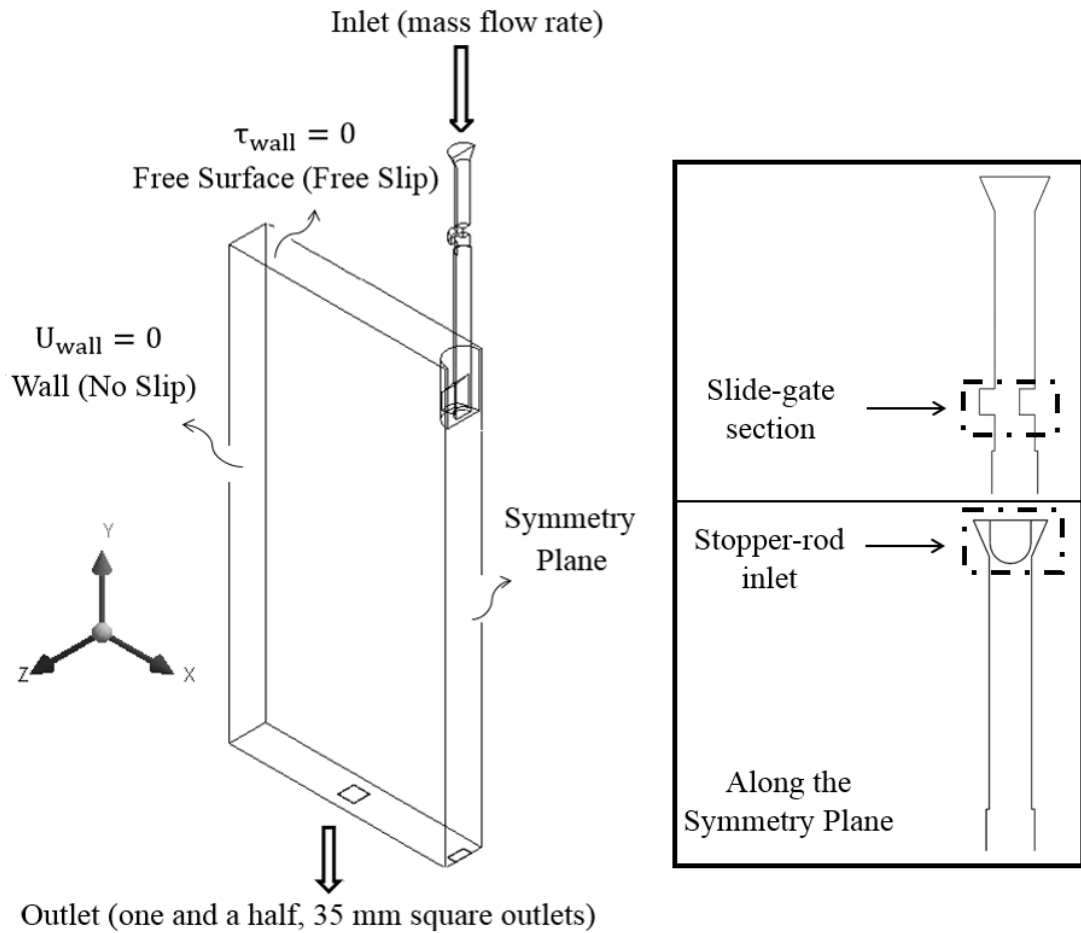


Figure 3. 1 Typical simulation domain and boundary conditions used in CFD models

3.2 The Mesh and Solution Parameters

The unstructured grid for the whole domain consisted of 3D tetrahedral elements and prismatic inflation layers. Patch conforming method was utilized for the creation of the mesh. The mesh is designed to get finer on the certain areas which are anticipated to have the greatest velocity gradients such as slide gate and port sections. Lower in

the mold region mesh elements starts to grow. The boundary layer was created using inflation option available within in the Meshing. The details of the meshes used in the mesh independence study is tabulated in Table 3.2. The mesh independent study was only performed for the slide gate controlled geometry, for the stopper rod controlled geometries very similar meshes were utilized. Samples from the slices of the mesh at slide gate, SEN inlet and stopper rod inlet regions along the symmetry plane are illustrated in Figure 3.2.

Table 3. 2 Summary of mesh independence study

Algorithm	Tetrahedrons and Prismatic Elements					
Method	Patch Conforming					
	Mesh 1	Mesh 2	Mesh 3	Mesh 4	Mesh 5	Mesh 6
Nodes	391724	796612	900852	1059852	1385712	1972591
Elements	1030945	2439675	3101733	4023953	5114789	8887628
Maximum Skewness	0.90	0.89	0.89	0.88	0.87	0.87
Minimum Orthogonal Quality	0.14	0.15	0.15	0.17	0.17	0.18

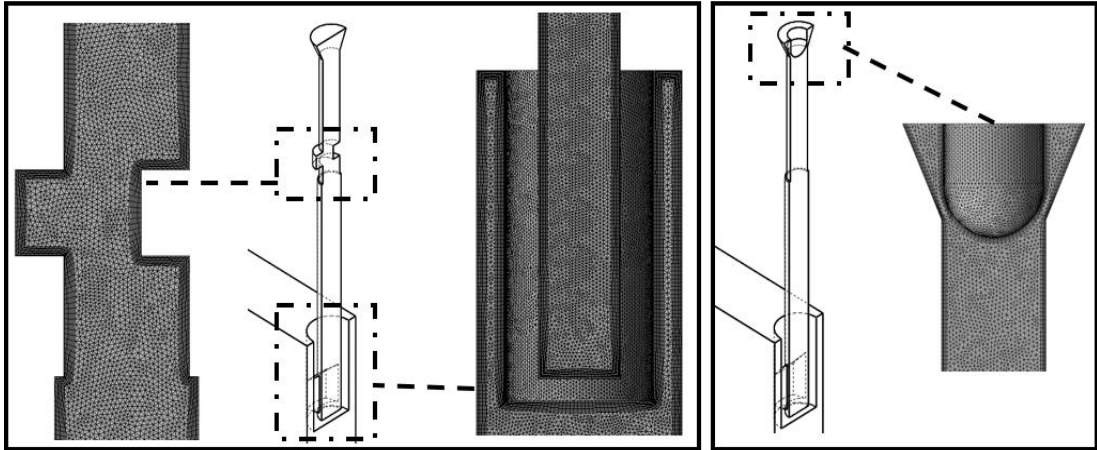


Figure 3.2 Slices of the mesh parallel to the side wall at slide gate, SEN and stopper rod inlet respectively

The mesh independency study was performed to make sure the solutions were independent of element number. The element number was increased until the solution did not change more than 1 %. The standard $k-\epsilon$ turbulence model was used for the mesh independence study. Second order upwind discretization scheme was utilized for spatial discretization of the momentum, turbulent kinetic energy and the turbulent dissipation rate. Second order upwind method was selected because it is known to yield more accurate results than the first order upwind scheme for tetrahedral grids. SIMPLE algorithm was the chosen pressure-velocity coupling scheme.

A typical simulation of whole domain took approximately 13 hours of computing time. The residual values of the velocity components are plotted to check the convergence behavior, Figure 3.3 represent a sample plot of the residual values for a standard $k-\epsilon$ simulation. The ultimate degree of convergence of the solutions were determined by the monitor points located on several locations within the mold. The velocity magnitudes on the monitor points were plotted and the convergence of the solutions were decided on their trend to change. Figure 3.4 demonstrates the convergence history of two selected monitor points: First one on meniscus region and the second one at port exit plane.

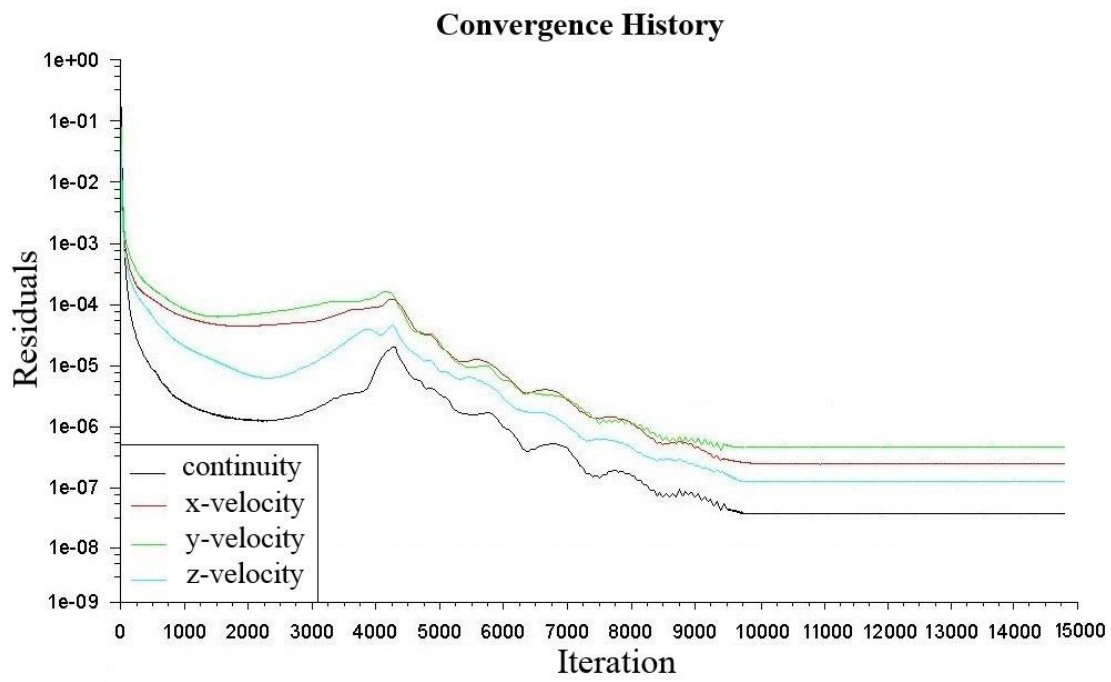
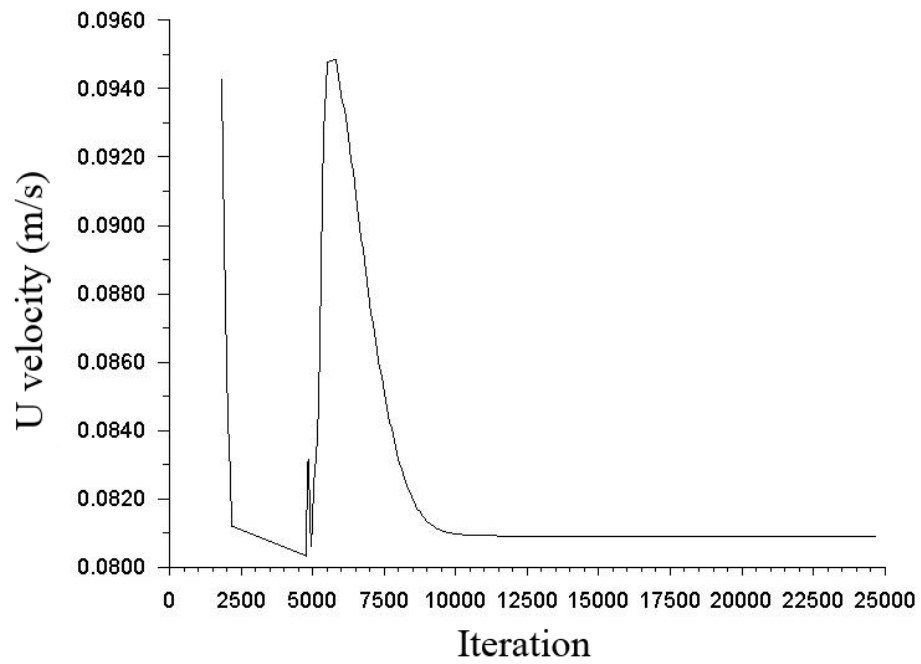


Figure 3.3 Convergence history of a typical simulation with standard k- ϵ turbulence model

a

Monitor Point at Meniscus Region



b

Monitor Point at Port Exit Plane

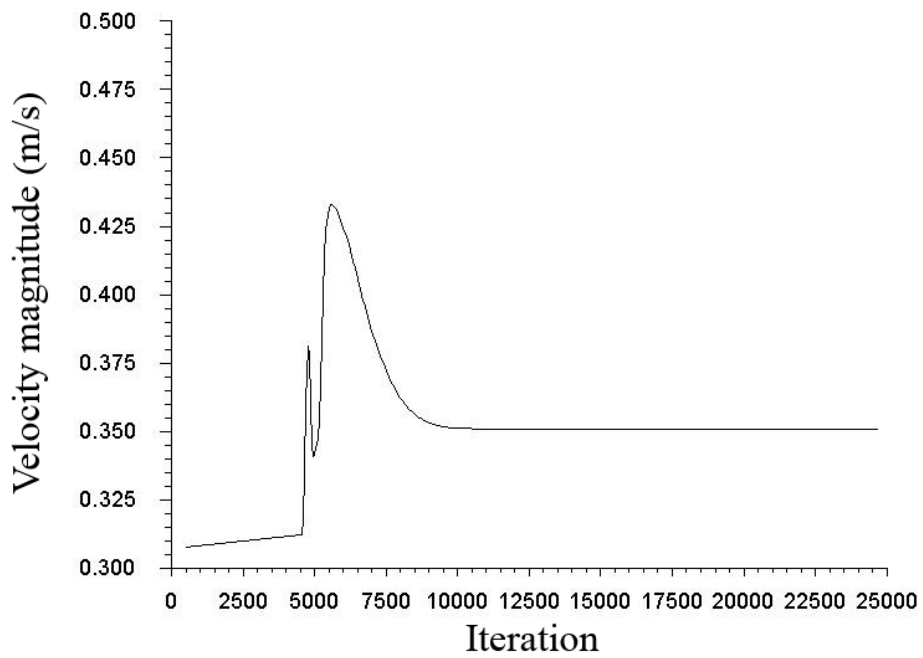


Figure 3.4 Sample monitor point results at a) meniscus region, b) port exit plane

3.3 Turbulence Models

The flow in the mold of continuous casting machines is highly turbulent. In order to model this turbulent flow, a suitable turbulence model needs to be identified. Fluent offers different turbulence models varying from simple to highly complex in regard to the modeling part of turbulence nature of the flow. In this study, based on the studies in literature, the performance of three different turbulence models were evaluated and compared to the water model test results. The selected turbulence models were standard k- ϵ , realizable k- ϵ and k- ω SST models. For the k- ω SST model the mesh was modified in order to keep y^+ value under 1. The first layer thickness in the inflation layer was decreased and quick simulations were performed to determine the current y^+ value. Once the required y^+ value is obtained the final simulations were performed. For all three models, the Mass Conservation Equation and the Momentum Conservation Equation were solved [75].

$$\frac{\partial y}{\partial x} + \nabla \cdot (\rho \vec{v}) = 0 \quad (3.1)$$

$$\frac{\partial}{\partial t} (\rho \vec{v}) + \nabla \cdot (\rho \vec{v} \vec{v}) = -\nabla \rho + \nabla \cdot (\vec{\tau}) + \rho \vec{g} \quad (3.2)$$

Other equations solved within each turbulence model are provided below.

For Standard k- ϵ Model the turbulence kinetic energy, k, and its rate of dissipation, ϵ , are obtained from the following transport equations;

$$\frac{\partial}{\partial t} (\rho k) + \frac{\partial}{\partial x_i} (\rho k u_i) = \frac{\partial}{\partial x_j} \left[\left(\mu + \frac{\mu_t}{\sigma_k} \right) \frac{\partial k}{\partial x_j} \right] + G_k + G_b - \rho \epsilon - Y_M + S_k \quad (3.3)$$

$$\frac{\partial}{\partial t} (\rho \epsilon) + \frac{\partial}{\partial x_i} (\rho \epsilon u_i) = \frac{\partial}{\partial x_j} \left[\left(\mu + \frac{\mu_t}{\sigma_\epsilon} \right) \frac{\partial \epsilon}{\partial x_j} \right] + C_{1\epsilon} \frac{\epsilon}{k} (G_k + G_{3\epsilon} G_b) - C_{2\epsilon} \rho \frac{\epsilon^2}{k} + S_\epsilon \quad (3.4)$$

The turbulent viscosity, μ_t , is calculated as;

$$\mu_t = C_\mu \rho \frac{k^2}{\varepsilon} \quad (3.5)$$

In above equations, G_k, G_b demonstrate the generated turbulent kinetic energy due to the mean velocity gradient and buoyancy respectively. $C_{1\varepsilon}, C_{2\varepsilon}, C_{3\varepsilon}$ are constants and S_k, S_ε are used-defined source terms. Y_M points out the contribution of the fluctuating dilatation in compressible turbulence to the overall dissipation rate and finally $\sigma_\varepsilon, \sigma_k$ are turbulent Prandtl numbers for ε and k respectively.

The values of the constants in the above equations is as follows;

$$C_{1\varepsilon} = 1.44, C_{2\varepsilon} = 1.92, C_\mu = 0.09, \sigma_\varepsilon = 1.0, \sigma_k = 1.3$$

Similarly, Realizable k- ε Model solves the following transport equations in order to obtain the turbulence kinetic energy, k , and its rate of dissipation, ε ;

$$\frac{\partial}{\partial t}(\rho k) + \frac{\partial}{\partial x_j}(\rho k u_j) = \frac{\partial}{\partial x_j} \left[\left(\mu + \frac{\mu_t}{\sigma_k} \right) \frac{\partial k}{\partial x_j} \right] + G_k + G_b - \rho \varepsilon - Y_M + S_k \quad (3.6)$$

$$\frac{\partial}{\partial t}(\rho \varepsilon) + \frac{\partial}{\partial x_j}(\rho \varepsilon u_j) = \frac{\partial}{\partial x_j} \left[\left(\mu + \frac{\mu_t}{\sigma_\varepsilon} \right) \frac{\partial \varepsilon}{\partial x_j} \right] + \rho C_{1\varepsilon} S_\varepsilon - C_{2\varepsilon} \rho \frac{\varepsilon^2}{k + \sqrt{\nu \varepsilon}} + C_{1\varepsilon} \frac{\varepsilon}{k} G_{3\varepsilon} G_b + S_\varepsilon \quad (3.7)$$

$$\text{where, } C_1 = \max \left[0.43, \frac{n}{n+0.5} \right], \quad n = S \frac{\varepsilon}{k}, \quad S = \sqrt{2S_{ij}S_{ij}}$$

The turbulent viscosity, μ_t , is calculated as;

$$\mu_t = C_\mu \rho \frac{k^2}{\varepsilon} \quad (3.8)$$

In above equations, G_k, G_b demonstrate the generated turbulent kinetic energy due to the mean velocity gradient and buoyancy respectively. $C_{1\varepsilon}, C_{2\varepsilon}, C_{3\varepsilon}$ are constants and S_k, S_ε are used-defined source terms. Y_M points out the contribution of the fluctuating dilatation in compressible turbulence to the overall dissipation rate and finally $\sigma_\varepsilon, \sigma_k$ are turbulent Prandtl numbers for ε and k respectively.

The values of the constants in the above equations is as follows;

$$C_{1\varepsilon} = 1.44, C_{2\varepsilon} = 1.9, \sigma_\varepsilon = 1.0, \sigma_k = 1.3$$

The shear-stress transport (SST) k- ω Model the turbulence kinetic energy, k, and specific rate of dissipation, ω , are obtained from the following transport equations;

$$\frac{\partial}{\partial t}(\rho k) + \frac{\partial}{\partial x_i}(\rho k u_i) = \frac{\partial}{\partial x_j} \left[\Gamma_w \frac{\partial k}{\partial x_j} \right] + \widehat{G}_k - Y_k + S_k \quad (3.9)$$

$$\frac{\partial}{\partial t}(\rho \omega) + \frac{\partial}{\partial x_i}(\rho \omega u_i) = \frac{\partial}{\partial x_j} \left[\Gamma_w \frac{\partial \omega}{\partial x_j} \right] + G_w - Y_w + D_w + S_w \quad (3.10)$$

The effective diffusivities an the turbulent viscosity, μ_t , is calculated as;

$$\Gamma_k = \mu + \frac{\mu_t}{\sigma_k} \quad (3.11)$$

$$\Gamma_w = \mu + \frac{\mu_w}{\sigma_w} \quad (3.12)$$

$$\mu_t = \frac{\rho k}{w} \frac{1}{\max \left[\frac{1}{a}, \frac{SF_2}{a_1 w} \right]} \quad (3.13)$$

In above equations, \widehat{G}_k demonstrates the generated turbulent kinetic energy due to the mean velocity gradient. Γ_w, Γ_k represent the turbulent diffusivity of w and k respectively and Y_w, Y_k point out the dissipation of w and k due to turbulence. S_k, S_w are used-defined source terms, D_w is the cross-diffusion term and G_w show the generation of w.

3.4 Flow Controller Effect

There are two common flow controller techniques to regulate the flow from the tundish to the mold. In order to observe the effect of flow controller on mold flow structure, slide gate and stopper rod controlled geometries were simulated under same throughput condition. Different controller openings were also simulated in order to quantify the effect of opening fraction on the mold flow. Five different slide gate opening fractions were simulated. The area and linear fraction openings, f_A , f_L , of slide gates simulations are tabulated in Table 3.3. Later, different stopper rod openings simulations were also performed to ultimately compare the performances of different flow rate control mechanisms on the mold flow structure. The stopper rod openings are tabulated on Table 3.4. Opening percentage of stopper rods are also calculated by dividing the area of the cross section from where distance R is defined to the nozzle bore area. The illustration of stopper rod and slide-gate openings are previously given in Figure 1.5 and Figure 1.6 respectively.

Table 3. 3 Slide gate opening parameters

Case Number	Case 1	Case 2	Case 3	Case 4	Case 5
Area Fraction	30%	40%	50%	60%	70%
Linear Fraction	41%	52%	60%	68%	76%

Table 3. 4 Stopper rod opening parameters

Case Number	Case 1	Case 2	Case 3	Case 4	Case 5
Distance L (mm)	23 mm	25 mm	27 mm	29 mm	31 mm
Distance R (mm)	6.66 mm	5.27 mm	4 mm	2.88 mm	1.94 mm
Area Fraction	81%	69%	57%	46%	35%

CHAPTER 4

RESULTS AND DISCUSSION

In this chapter, first, the mesh independency study is summarized. Then the performance of three different turbulence models is evaluated and the models are validated against the water model test results. Based on this evaluation, suitable turbulence model is selected to be used for the rest of the present study. Finally, to quantify the effect of flow controller type and their opening ratios on mold flow structure, the stopper rod and slide gate controlled domains are simulated and compared at different opening levels.

4.1 Mesh Independency Study

In order to reach a mesh independent solution, the grid was refined at each time, and six different mesh topologies were constructed. The coarsest mesh has 391724 nodes and 1030945 elements whereas the finest mesh consist of 1972591 nodes and 8887628 elements. The details of the mesh are tabulated in Table 3.2 in Chapter 3. The normalized velocity vectors for two sample meshes are plotted at the center plane, parallel to the wide face of the mold as shown in Figure 4.1. In constructing the Figure 4.1, the lengths of vectors are normalized and thus do not contain velocity magnitude information whereas the greyscale indicates the magnitude of the velocity vectors shown on the left side of the figure. Despite the fact that the two meshes predict the double roll flow pattern successfully, a slight difference is detected in the overall flow pattern. The jet exiting the nozzle ports is stronger in Mesh 2 and Mesh 2 has also higher meniscus velocities. For comprehensive comparison, Figure 4.2 is constructed

for U velocity magnitudes along the meniscus region at the centerline of the narrow face parallel to the broad face of the mold. The figure demonstrates the absolute value of U velocities. The results indicate that velocity values differ up to 28% between meshes 1-3. The velocity trends also show a dramatic change between meshes 1-3. Starting from Mesh 4 however, the velocity magnitudes do not vary more than 1%. Moreover, Figure 4.2 demonstrates that the flow fields are symmetrical within the simulation domain. Further comparisons of the results corresponding to different mesh densities are shown in Figure 4.3 where the velocity magnitudes are plotted at three different locations of the port exit. The sketch on the right hand side of the figure presents the locations of the data lines along which the velocity magnitudes are obtained. The plotted velocities are at the center plane and 6 and 12 mm away from the center plane. The velocity magnitudes are calculated by using the u and v components of the velocity only, as the experimental data provided. The results display that the velocity magnitudes and the general trends show great variations within the range of 6 mm. This is directly linked with the existence of strong circulation in the port exit arising from the slide gate impact on the flow structure. Figure 4.3 demonstrates consistent results with the results indicated in Figure 4.2. As can be seen in the Figure 4.3 the velocities show great variations between meshes 1-3 raising up to 25%. The predictions of the meshes 4-6 are almost equal with the results do not show variations more than 1%. Considering these results it can be concluded that a mesh independent solution is achieved starting from the mesh 4. Therefore, Mesh 4 emerges as the selected mesh for this study as it contains the least nodes and element numbers among the meshes 4-6.

4.2 Turbulence Model Comparison

In this part of the study, the results of three different turbulence models, standard k- ϵ , realizable k- ϵ and k- ω SST models, are presented and compared against experimental results. Utilizing the symmetry in the domain only the half of the geometry was

simulated in order to reduce the computation time. The normalized velocity vectors for three different turbulence models are plotted at the center plane, parallel to the wide face of the mold as shown in Figure 4.4. The figure indicates that all three turbulent models succeeded in obtaining the double roll flow pattern within the mold. The strong upper circulation regions are apparent, particularly for the standard and realizable $k-\epsilon$ models. The velocity magnitudes show that the standard and realizable $k-\epsilon$ models predict strong upper circulation with weak lower circulation, whereas, SST model predicts strong lower circulation with weak upper circulation.

The velocity magnitudes in the meniscus region are plotted at the center plane of the narrow face parallel to the broad face of the mold, as demonstrated in Figure 4.5. The figure demonstrates that meniscus velocity predictions differ in each turbulence model in terms of both magnitude and trend. The realizable $k-\epsilon$ model prediction has the greatest velocity magnitudes whereas the $k-\omega$ SST model has the lowest. In order to further distinguish the differences of the results, the velocity magnitudes are plotted at three locations of the port exit in Figure 4.6. Figure 4.6 was created using the same approach of the Figure 4.2, once again the schematic illustration of port exit plane is provided on the right side of the figure. Figure 4.6 provides the velocity magnitude predictions of three turbulence models along with the experimental data from the literature [10, 50]. The PIV results of the experiments are presented at both center and 12 mm away from the center planes [10, 50]. It is important to mention that finite thickness of the laser sheet in PIV experiments varies approximately from 1 to 5 mm, which also determines the resolution of the experiment. It should be noted that the PIV results are obtained by taking the average of the velocity magnitudes within the thickness of the PIV laser. Figure 4.6 demonstrates that the velocity predictions of turbulence models display great shifts within a distance of 12 mm. In the first 6 mm they experience a velocity decrease up to 45% in average. However, later in the second 6 mm they perform a velocity increase up to 50% in average. The possible mechanisms responsible from these variations are discussed previously in the mesh independency chapter. These velocity shifts clearly shows that the resolution of the turbulence model predictions are superior to those of PIV experiments. Therefore, in order to better

discuss the results, average of the bot PIV results and turbulence model predictions are calculated. In Figure 4.7 the average of these three velocity magnitudes for each turbulence model are compared to the averages of PIV data. As shown Figure 4.7 the results of the all three turbulence models show very close trends with experimental data, and their predictions are almost equal to those of PIV results. Particularly considering the resolution of PIV experiments, the predictions of all three models are quite accurate. The standard k- ϵ model predicts slightly larger velocity magnitudes compared to the predictions of other turbulence models.

Further comparisons of turbulence models are based upon the jet angle characteristics. Two types of jet angles: slice jet angle and overall jet angle are calculated and compared in Table 4.1. The overall jet angle, or simply the jet angle, is the average angle of the all velocity data on nozzle exit plane for x and y components of the velocity, the slice jet angle defines as the simple arithmetic mean of the velocity components on a specific plane [10, 50]. The calculation of the overall jet angle is available in Appendix A. Table 4.1 indicates that standard k- ϵ and k- ω SST models predictions are very close to those of PIV measurements, realizable k- ϵ model on the other hand, predicts slightly larger values.

For the final comparison Figure 4.8 is constructed, where both the velocity magnitudes along jet and the meniscus velocity predictions at single point 20 mm below the meniscus for three different turbulence models along with the LES model predictions and experimental measurements are demonstrated. The study which supplies the experimental data [50], provides the time history of the PIV and LES data, therefore in order to compare them with the predictions of the three turbulence model, the mean of the LES and PIV results are calculated and shown in Figure 4.8b. Figure 4.8a and 4.8b demonstrate that the predictions by three turbulence models are reasonable compared to the experimental data and averaged LES simulation results. Considering the speed of jet along its direction, the turbulence models predict close values to those PIV measurements, however LES model prediction are better compared to URANS model predictions in terms of capturing the jet velocity trend of the PIV results. The predictions of the k- ϵ realizable model are closer to the LES predictions. Considering

the meniscus velocity predictions shown in Figure 4.8b, the standard k- ϵ model result is almost equal to the mean of the PIV measurements. The k- ω SST model also predicts close values to those of the PIV measurements. It is also important to mention that, considering the Figures 4.8a and 4.8b, it is reported that despite predicting higher jet speed, LES model has relatively lower meniscus velocity.

Carrying on the study to determine the effects of flow rate controllers on mold flow, one turbulence model was chosen based on the aforementioned comparisons. The overall conclusions of previous comparisons lead us to accept standard k- ϵ and k- ω SST model predictions as accurate. In addition, the fast and easy converging behavior of the standard k- ϵ model during solutions made this model to be used in further calculations.

4.3 Influence of Flow Controller

This part of the study focuses on the effect of the selected flow controllers, slide gate and stopper rod systems, and their opening levels on the flow structure inside the SEN and the mold.

For the slide gate controlled domain five different opening fractions were simulated. Mentioned earlier, ladle changes result in liquid steel level changes in tundishes and the flow rate controller opening is increased to reduce the pressure drop across the opening. The particular interest here is to investigate the opening effect on meniscus region under the constant throughput casting operation for different flow rate controller openings. The area and linear fraction openings of slide gates simulations are tabulated in Table 3.3. The simulated area opening fractions of the slide gates range from 30% to 70% in the present study.

The normalized velocity vectors on central plane for each of the five cases are demonstrated in Figure 4.9. The aforementioned approaches, used for constructing Figure 4.1, were adopted for Figure 4.9. Figure 4.9 shows that the formation of double

roll flow pattern is evident in all five cases. Qualitatively, similar flow patterns are observed. Further comparison of the results for different cases is shown in Figure 4.10, where velocity fields in the SEN are presented. Figure 4.10a demonstrates the velocity vectors at slide gate region on symmetry plane where Figure 4.10b and Figure 4.11c illustrate the velocity vectors at port region on the symmetry plane and on the port exit plane, respectively. The velocity scale for each one is shown on the left side of the corresponding image.

As shown in Figure 4.10a the recirculation zones around the slide gate sections of the nozzle get smaller with the increasing opening fractions. Figure 4.10b and 4.10c show that the one-sided recirculation zones within the port exist for all of the five slide gate mechanisms. Figure 4.10c illustrates similar results to Figure 4.10a, since it demonstrates the adverse relation between the slide-gate opening fraction and the recirculation zones.

The velocity magnitudes at meniscus region are plotted for five different slide gate cases and shown in Figure 4.11. Data line is created from the center of the SEN to the side wall. The velocity magnitudes show that as the slide gate opening increases, the meniscus velocities also increase. Up to 30% increase in meniscus velocities can be achieved at constant throughput just altering the slide gate opening. It is also important to mention that the maximum velocity point moves toward SEN as the gate opening increases.

Similar to slide gate controlled domain, five different opening fractions were simulated under the same throughput conditions, for stopper rod controlled domain. The opening distances of stopper rod simulations are illustrated in Figure 1.5 and tabulated in Table 3.4. The simulated opening fractions of the stopper rods range from 35% to 81%.

The normalized velocity vectors on central plane of the mold parallel to broad face for five different stopper rod openings are illustrated in Figure 4.12. Figure 4.12 shows that the formation of double roll flow pattern is evident in all five cases. Both qualitatively and quantitatively very similar flow patterns are obtained.

The effect of stopper rod on flow fields within the SEN and inlet of the UTN is illustrated in Figure 4.13. Figure 4.13a shows the velocity vectors at stopper rod inlet on symmetry plane where Figure 4.13b and Figure 4.13c illustrate the velocity vectors at port region on the symmetry plane and on the port exit plane, respectively. The velocity scale for each one is shown on the left side of the corresponding image.

Figure 4.13a illustrates very similar flow fields around UTN inlet. Figure 4.13b and 4.13c show that the two-sided recirculation zones within the port exist for all of the five stopper rod cases. At this point there is great difference between slide gate and stopper rod controllers, since stopper rods produce two-sided almost symmetrical weak recirculation zones whereas, slide gate controllers produce one sided very strong recirculation zones at the bottom of the port as indicated in figures 4.10 and 4.13.

The velocity magnitudes at meniscus region are plotted for five different stopper rod openings and demonstrated in Figure 4.14. Data line is created from the center of the SEN to the side wall. The Figure 4.14 demonstrates no significant difference between the meniscus velocities indicating that meniscus velocities are not affected by the changes in the stopper rod opening fraction.

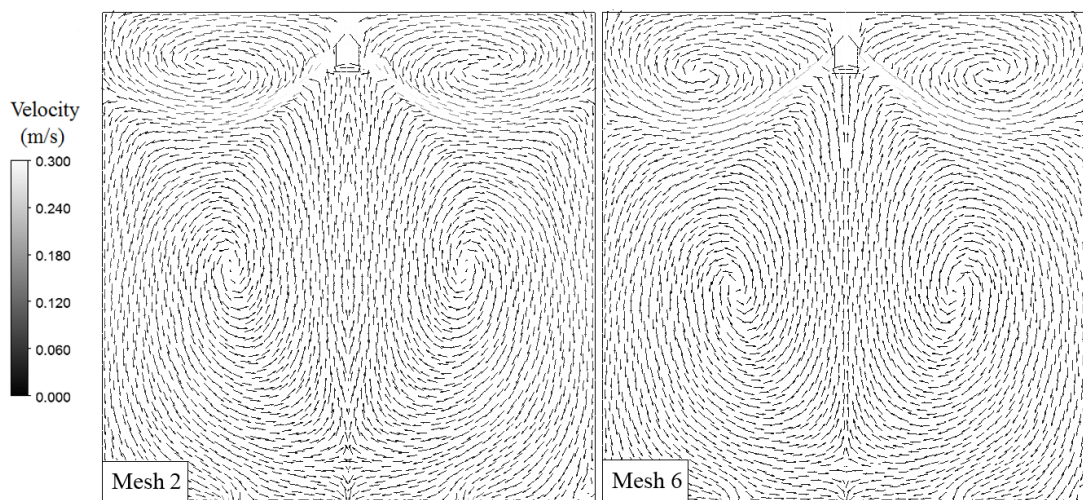


Figure 4.1 Normalized velocity vectors at the center plane of the mold for two different meshes

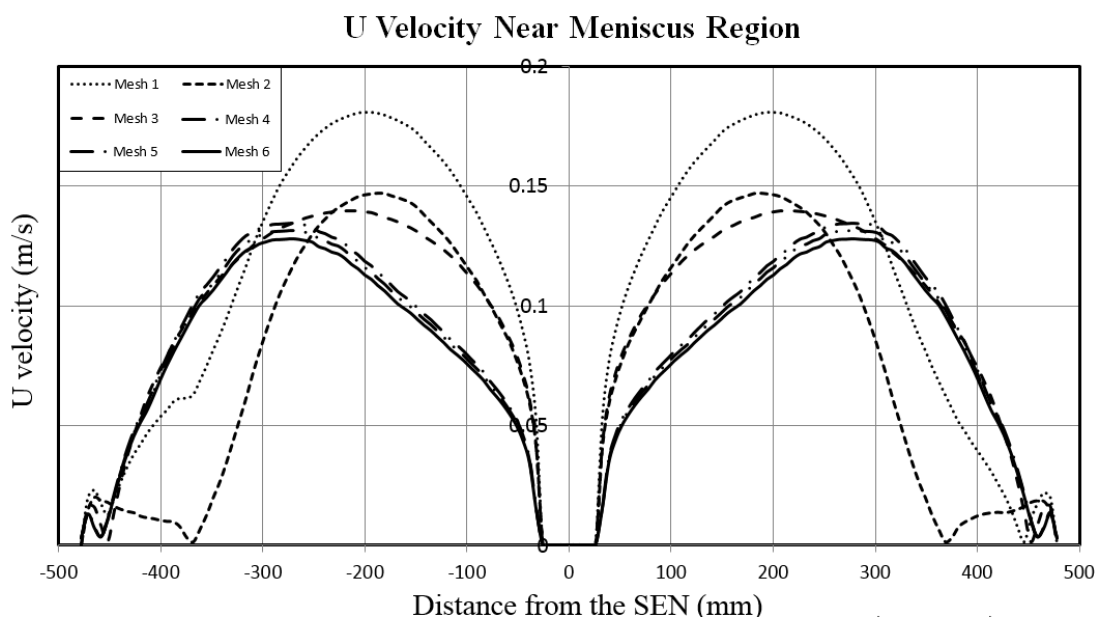
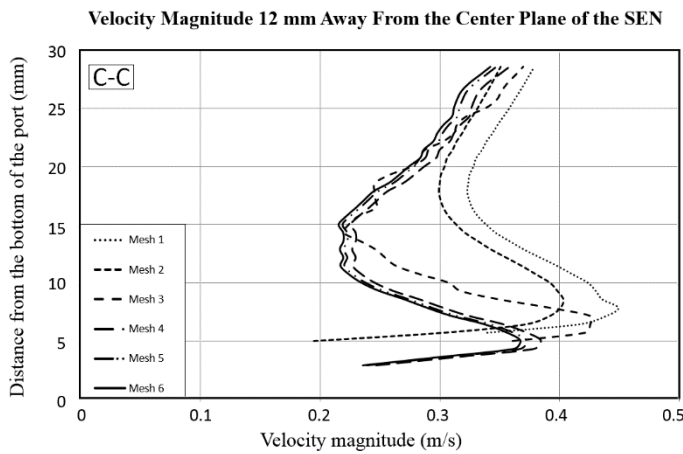
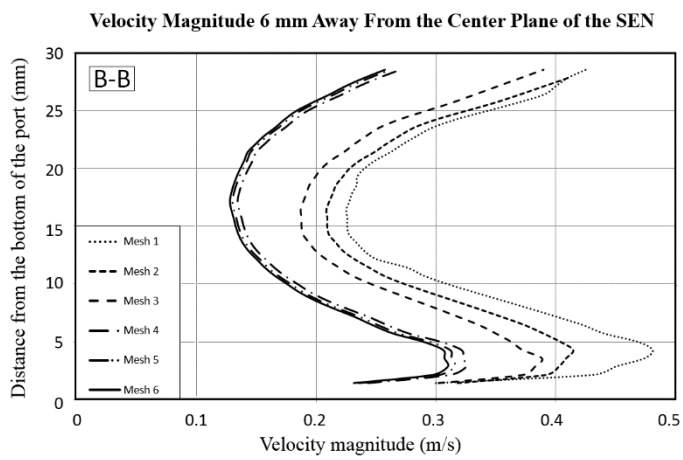
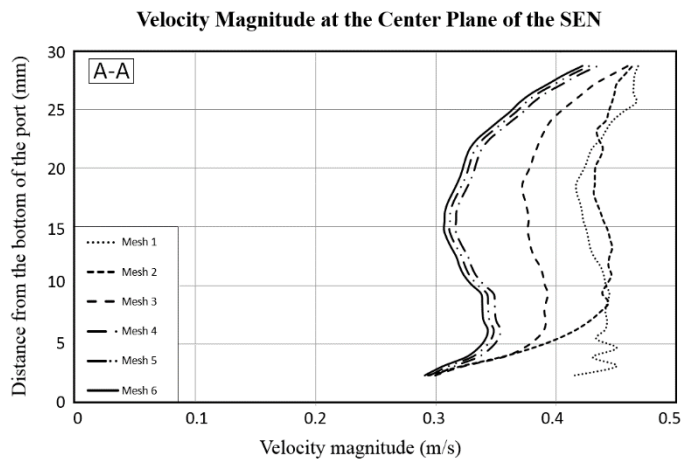


Figure 4.2 Meniscus velocities at the center plane of the SEN for six different meshes



Data lines on nozzle port

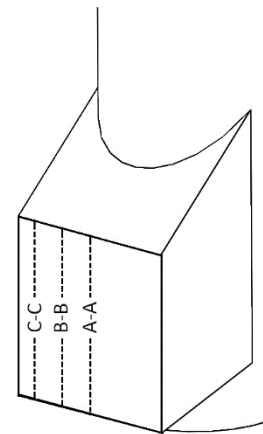


Figure 4.3 Velocity values for six different meshes (a) at the center of the port exit, (b) at 6 mm away from center of the port exit, (c) at 12 mm away from center of the port exit

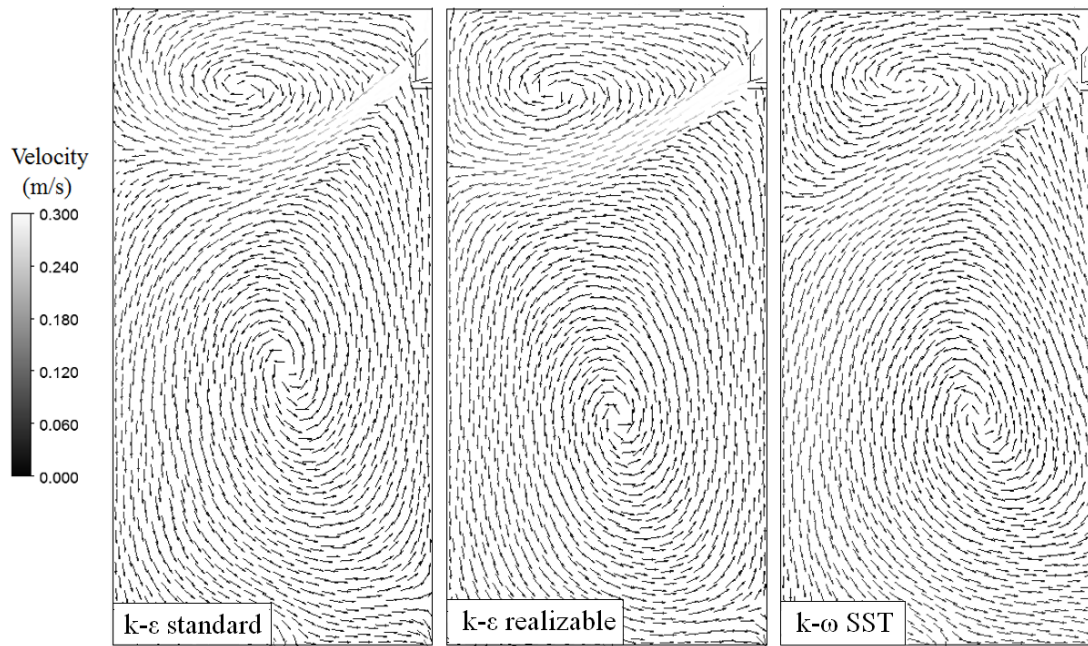


Figure 4.4 Normalized velocity vectors at the center plane of the mold for three different turbulence models

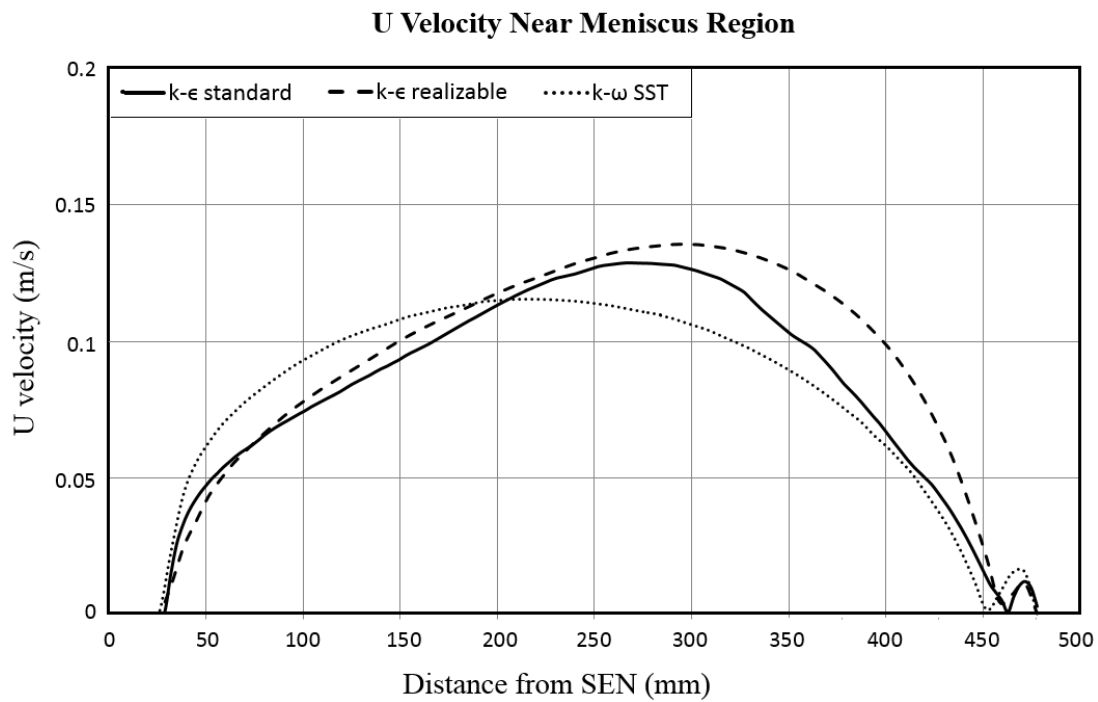
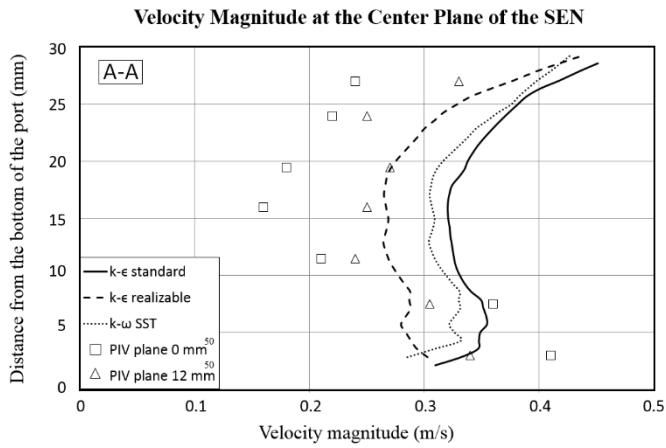


Figure 4.5 Meniscus velocities at the center plane of the SEN for three different turbulence models



Data lines on nozzle port

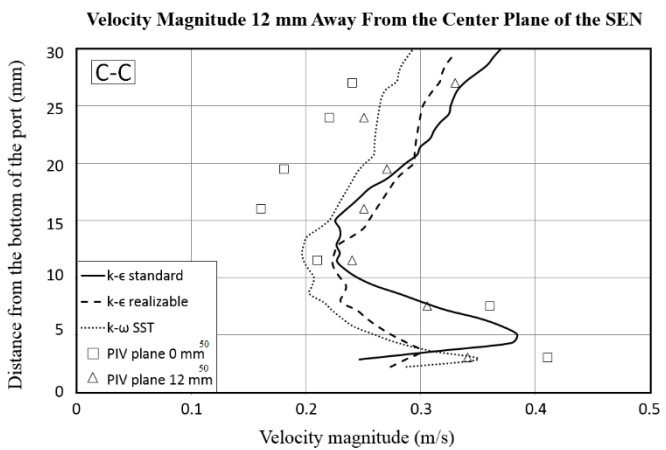
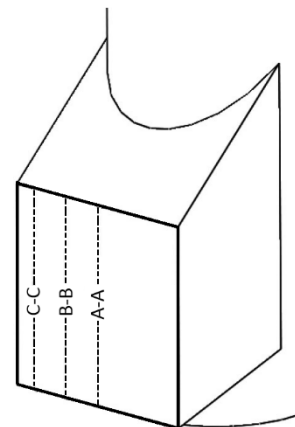
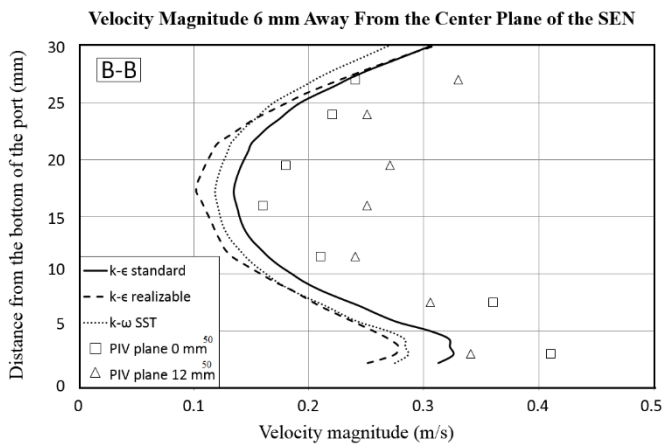


Figure 4.6 Velocity values for different turbulence models (a) at the center of the port exit, (b) at 6 mm away from center of the port exit, (c) at 12 mm away from center of the port exit

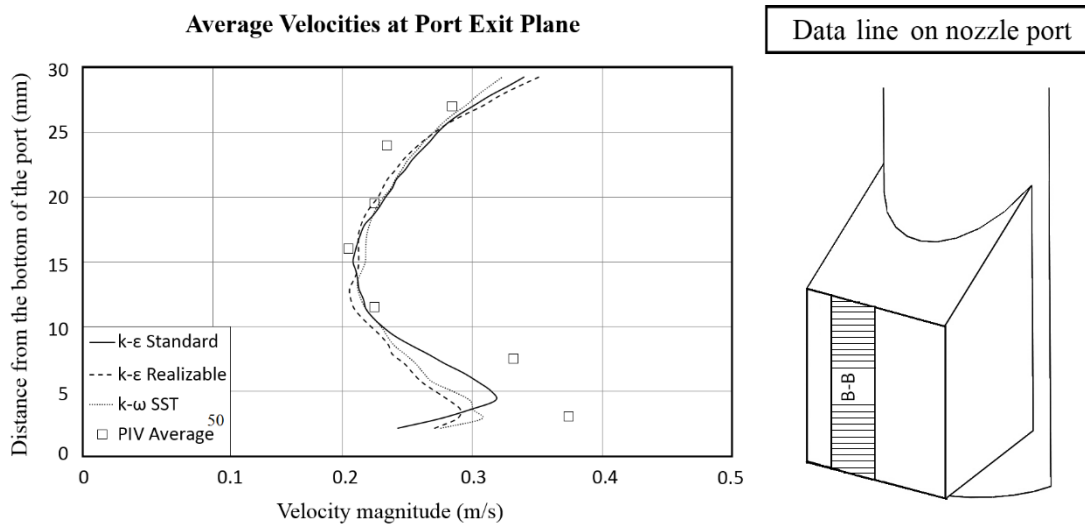
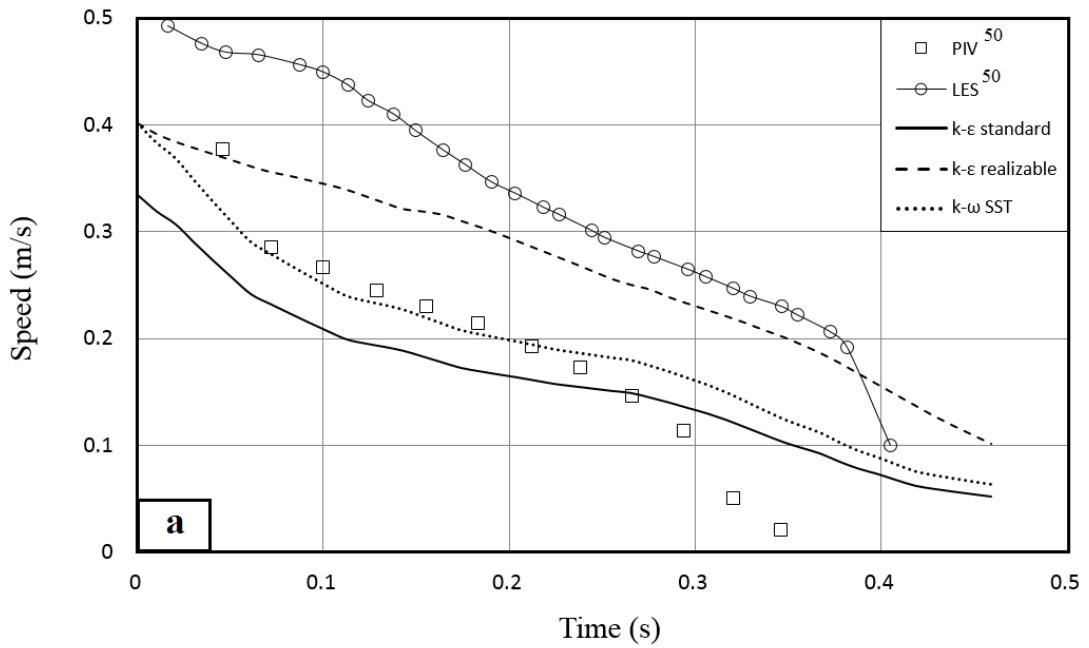


Figure 4.7 Average velocity values for three turbulence models and PIV data

Table 4. 1 Jet angle comparison

		Experimental Results ⁵⁰	k-ε Standard	k-ε Realizable	k-ω STT
Jet Angle		29°	31.02°	34.35°	31.80°
Slice Jet Angle	Center Plane	40.30° down	40.33° down	42.50° down	41.08° down
	12 mm Away Plane	22.8° up	21.48° up	23.36° up	21.14° up

Speed of Jet Along Its Direction



U Velocity 20 mm Below Meniscus Region

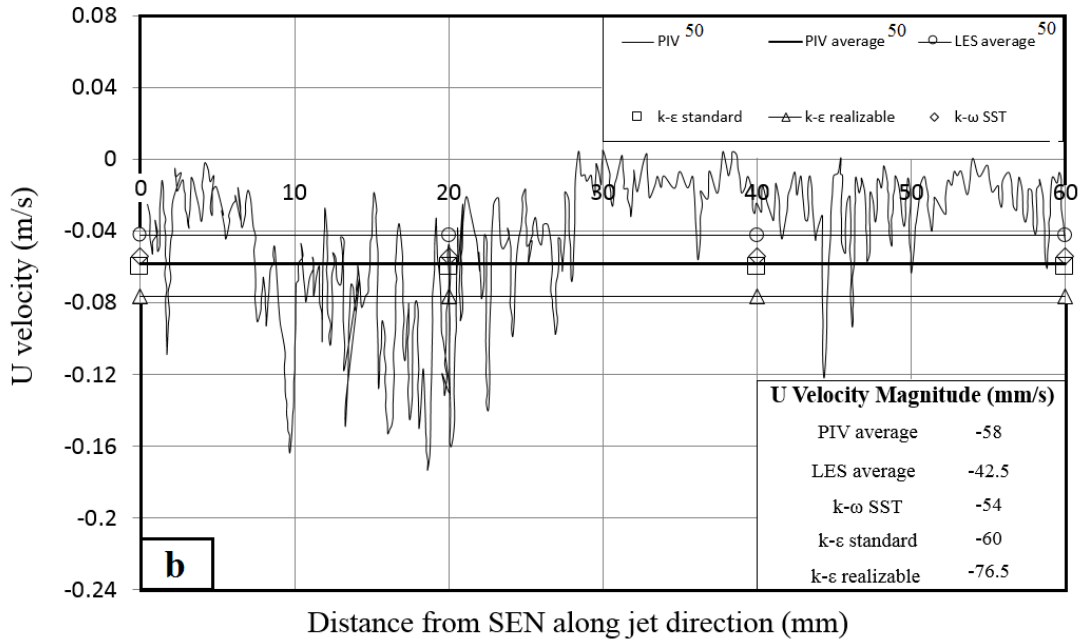


Figure 4.8 Evaluation of different turbulence models by (a) speed of jet along its direction, (b) u velocity values for meniscus region

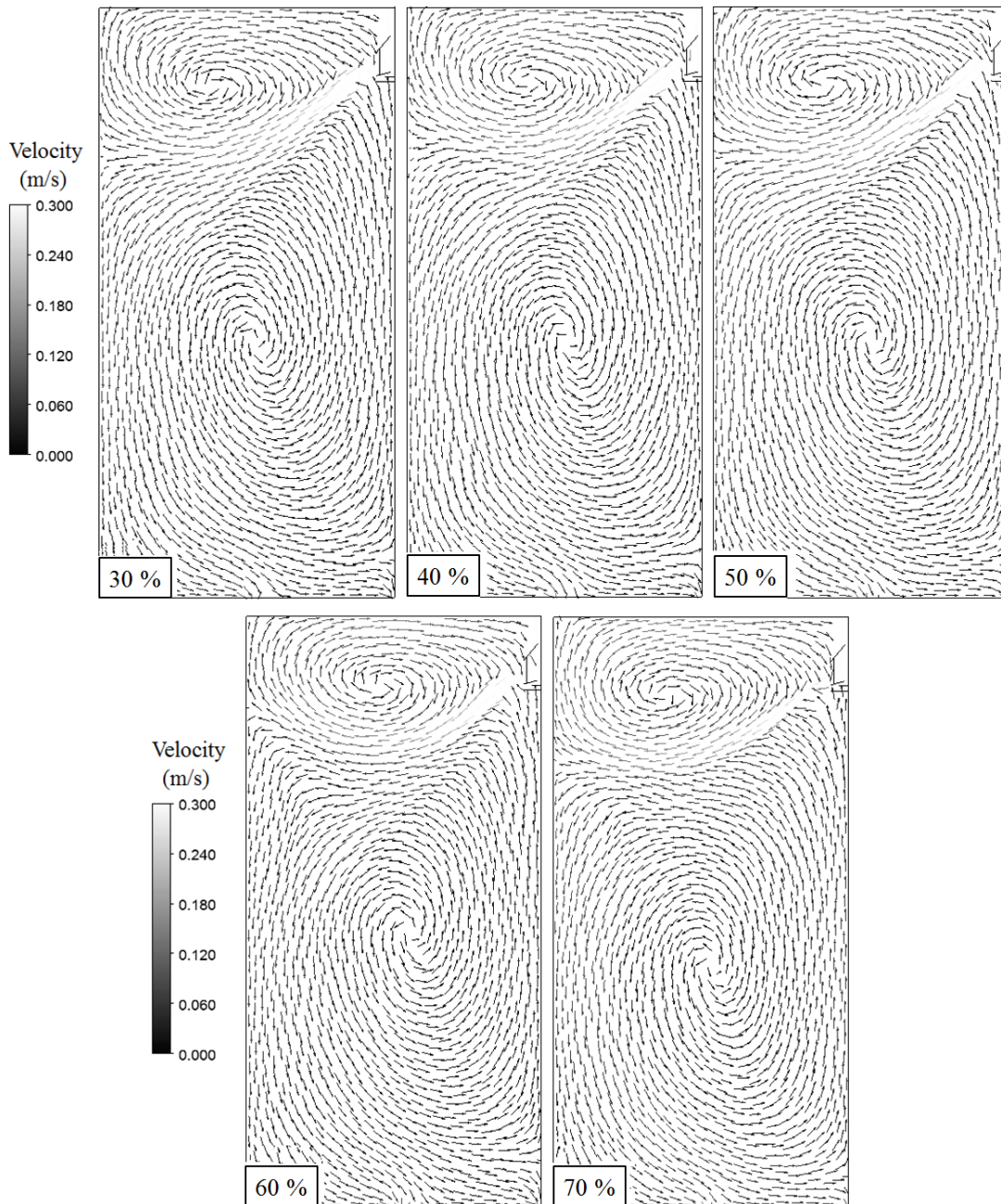


Figure 4.9 Normalized velocity vectors at the center plane of the mold for five different slide gate openings

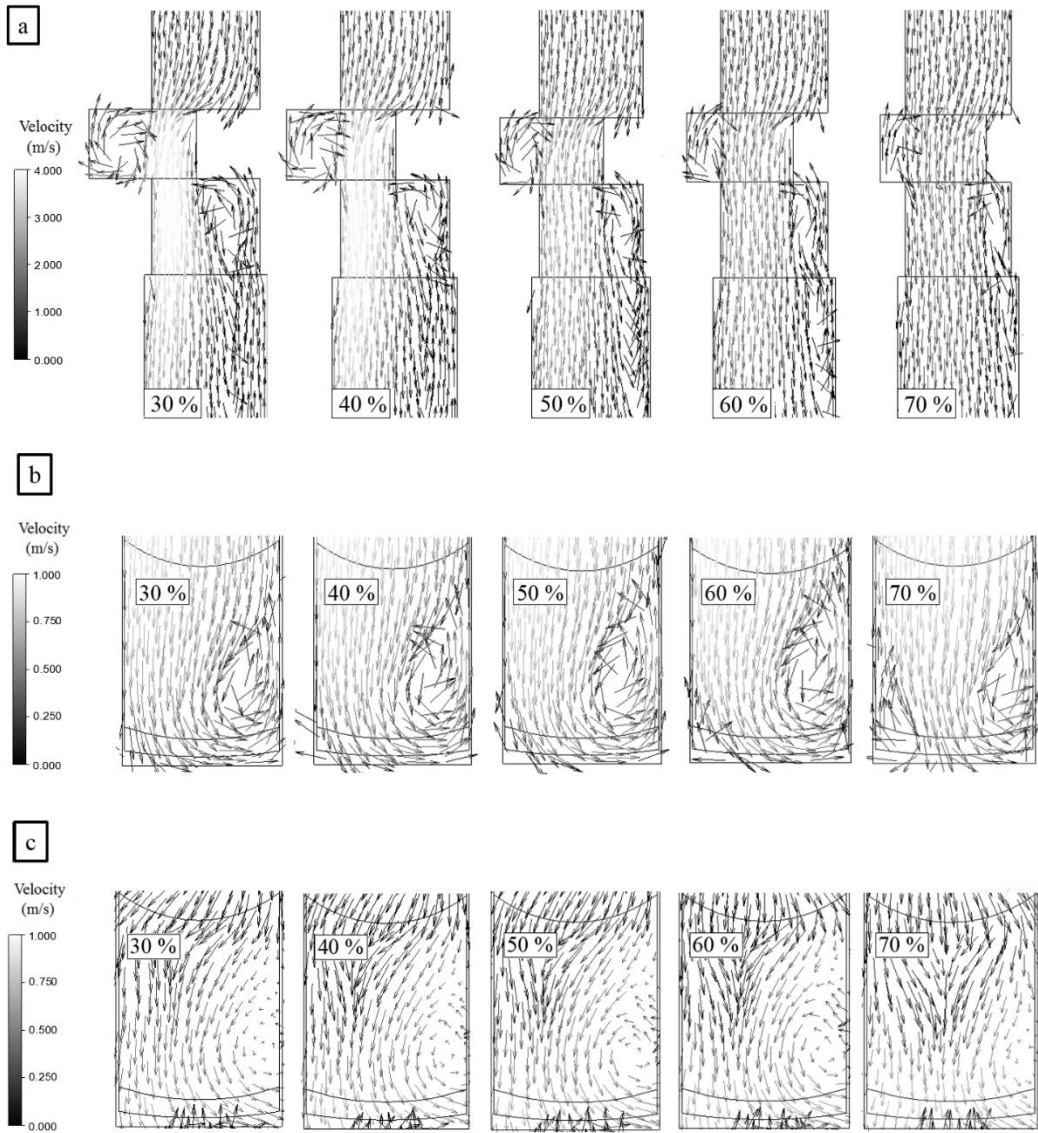


Figure 4.10 Velocity vectors (a) at slide gate region on the symmetry plane, (b) at nozzle region on the symmetry plane, (c) at nozzle region on the port exit plane

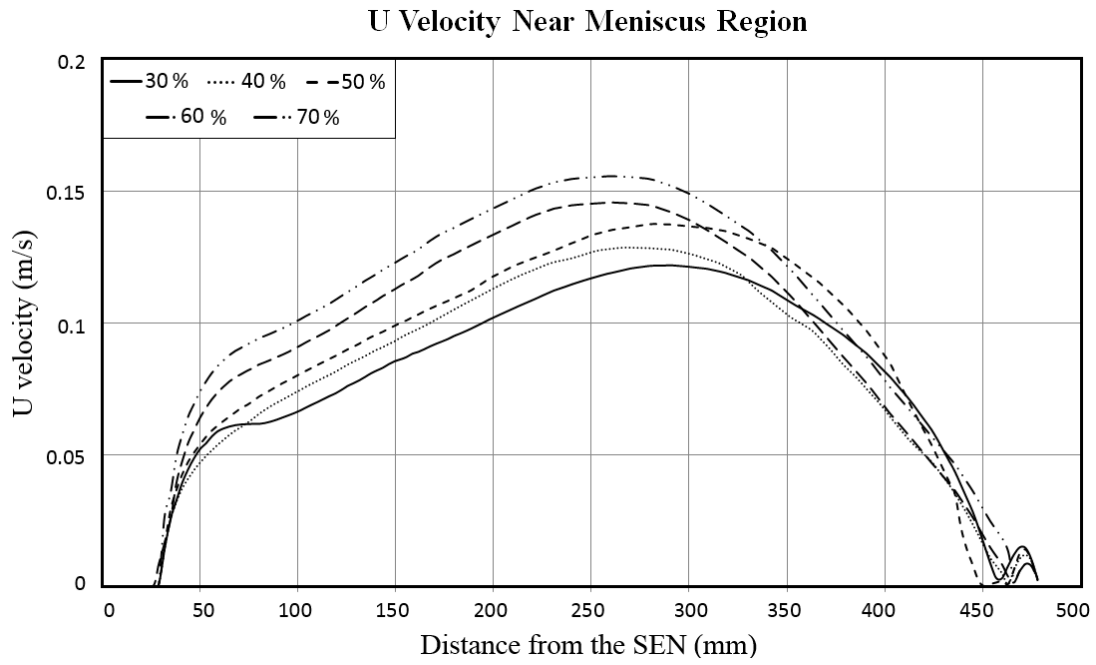


Figure 4.11 Meniscus velocities at the center plane of the SEN for five different slide gate opening

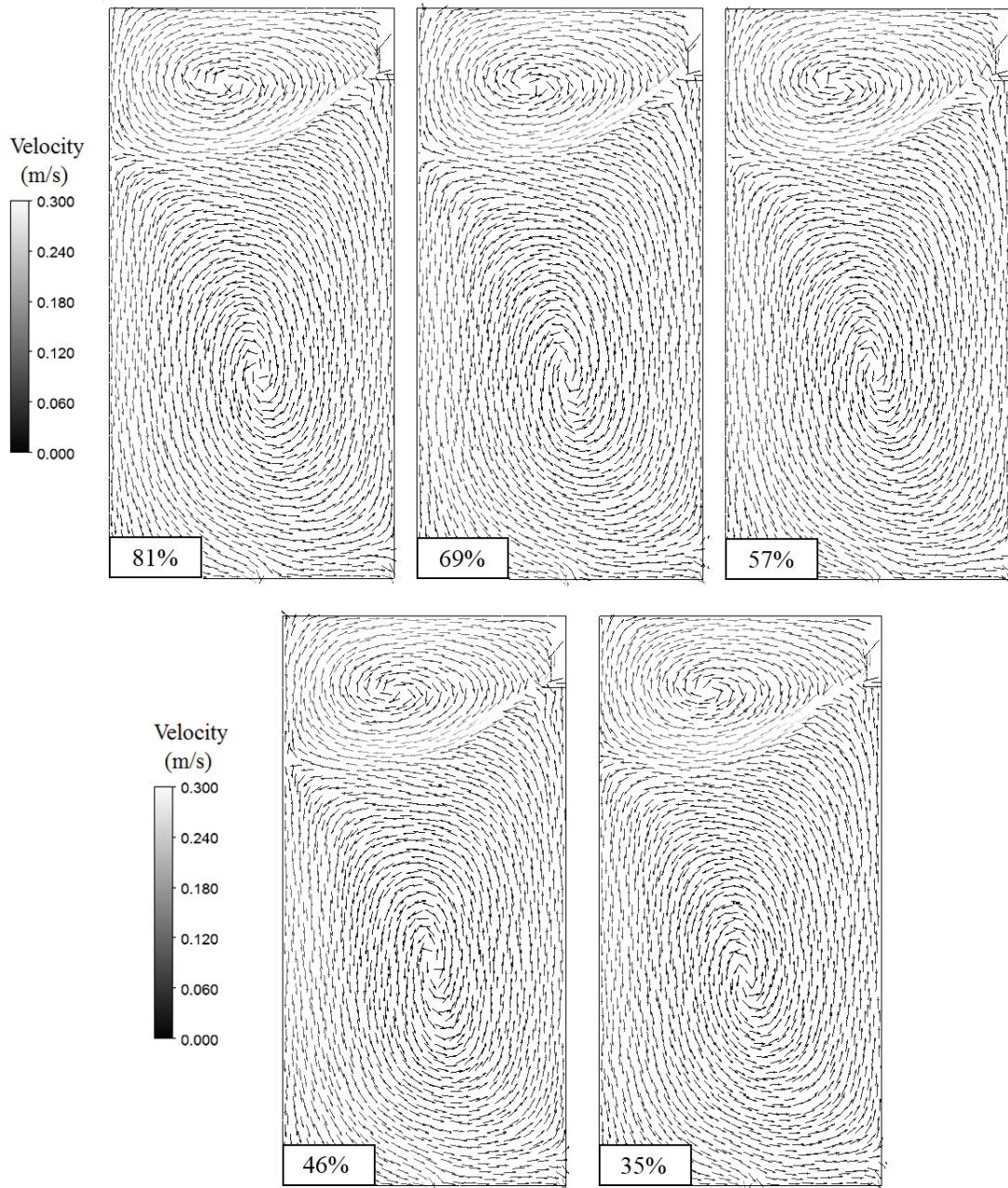


Figure 4.12 Normalized velocity vectors at the center plane of the mold for five different stopper rod openings

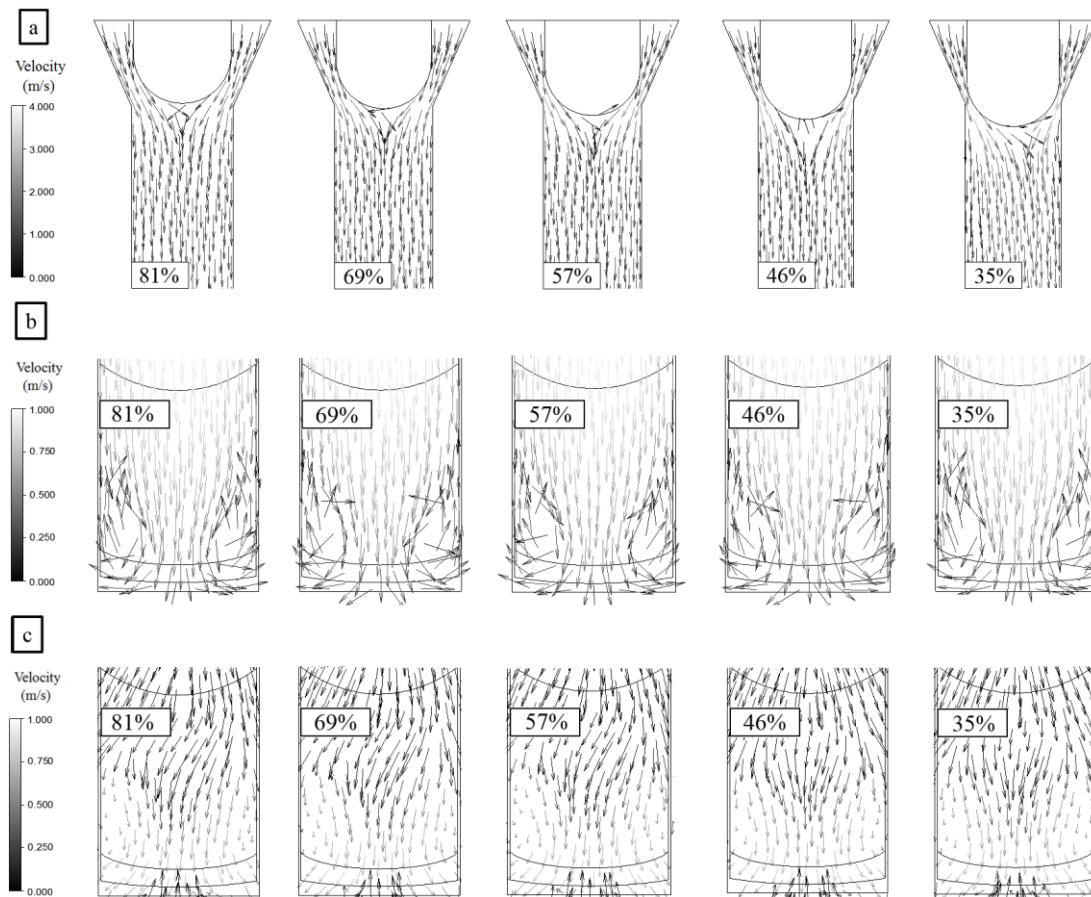


Figure 4.13 Velocity vectors (a) at stopper rod region on the symmetry plane, (b) at nozzle region on the symmetry plane, (c) at nozzle region on the port exit plane

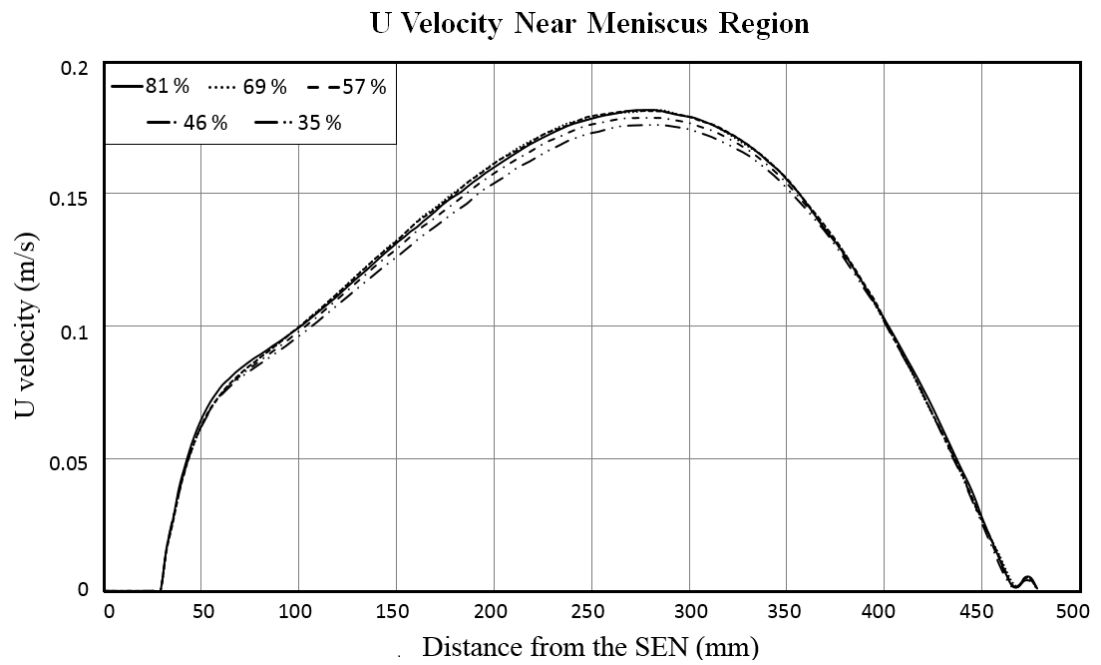


Figure 4.14 Meniscus velocities at the center plane of the SEN for five different stopper rod openings

CHAPTER 5

CONCLUSIONS

5.1 Summary and Conclusions

Ladle change operations in continuous casting machines result in liquid steel level changes in tundishes. During this transient event of production, the flow rate controller opening is increased to reduce the pressure drop across the opening, which helps to keep the mass flow rate constant for the reduced liquid steel level in tundish. Therefore, the effects of different opening levels for flow controllers on mold flow structure need to be understood.

The present study aims to investigate the effect of different flow controllers on mold flow structure using CFD modeling. In addition, the effect of flow controller opening on meniscus flow is quantified. A CFD model was developed for a water model, which had 0.4-scale geometry of the nozzle and the mold of an actual caster for steady state operation. For the constructed simulation domain a mesh independency study was performed. The results demonstrate that the mesh independent solution was reached with the mesh which do not alter the velocity predictions more than 1%. The resulting mesh contains both tetrahedral and prismatic elements and consists of approximately 1 million nodes and 4 million elements.

The performances of three different turbulence models, standard k- ϵ , realizable k- ϵ and k- ω SST, were compared and validated against PIV data available in literature. Despite all three models displayed good performances, one was selected due to its fast and easy converging performance. The standard k- ϵ model was used for the rest of the study to quantify the effect of different flow controllers and their opening levels on mold flow structure.

Five different opening fractions for both slide gate and stopper rod flow controllers were simulated for constant throughput condition. The results indicate that the flow structure within the mold, particularly meniscus region, is influenced by the alterations in the slide gate opening. Thus, for quality and castability purposes, adjusting the slide gate opening to obtain the fixed mold flow structure can be proposed. On the other hand, for a stopper rod controlled geometry, the flow structure and velocities in the meniscus region do not affected by the changes in the opening fraction of the controller indicating that, despite the level changes in the tundish, stopper rods can provide the same quality steel under same throughput condition.

5.2 Future Work

The present study investigates the effect of different flow controllers and their opening levels on mold flow structure with steady state CFD models. Aforementioned discussions regarding some of the meniscus flow problems such as mold level fluctuations and periodic oscillations are directly related to the unsteady flow behavior within the mold. Transient behavior of the mold flow has also significant influence on the final product quality. Thus, same analyses can be run with unsteady turbulence models and transient behavior of the mold flow can be captured. Particularly, the effects of different flow controllers and their opening levels on unsteady mold flow structure can be quantified.

In addition to the unsteady simulations, injection of argon gas and including heat transfer effects along with solidification simulations can also be investigated. Furthermore, the study can be carried one step further by modeling the steel-slag interface, hence more insights can be gained about the detrimental slag entrainment.

REFERENCES

1. Gursoy, K. A. and Yavuz, M. M., “*Mathematical Modeling of Liquid Steel Flow in Continuous Casting Machine*” IISS 2012, International Iron and Steel Symposium, April, Karabuk, Turkey, Volume 1 pp.99-105.
2. World Steel Association, “*World Steel in Figures 2012*”, 2012.
3. World Steel Association, “*World Steel in Figures 2013*”, 2013.
4. Thomas B.G., “*Continuous Casting*”, The Encyclopedia of Materials: Science and Technology., D. Apelian, ed., Elsevier Science Ltd., Oxford, UK, Volume 2, Oct. 31, 2000.
5. Szekeres E.S., “*Continuous Casting Systems-An Introduction*” Brimacombe Continuous Casting Course, May 2007, Vancouver, B.C Canada.
6. Wolf, M.M., “*History of Continuous Casting*” Steelmaking Conference Proceedings, 75, Iron & Steel Society, Warrendale, PA, 1992, pp. 83-137.
7. Okumura H., “*Recent Trends and Future Prospects of Continuous Casting Technology*”, Nippon Steel Technical Report No.61 April 1994.
8. Thomas B.G., “*Continuous Casting of Steel*”, Chapter 15 in Modeling for Casting and Solidification Processing, O. Yu, editor, Marcel Dekker, New York, NY, 2001, pp. 499-540.
9. Thomas, B. G., “*Fluid Flow in the Mold*”, Chapter 14 in Making, Shaping and Treating of Steel, 11th Edition, 5, Casting Volume, A. Cramb, ed., AISE Steel Foundation, Oct.2003, Pittsburgh, PA, 14.1-14.41.
10. Bai H., “*Argon Bubble Behavior in Slide-Gate Tundish Nozzles during Continuous Casting of Steel Slabs*” Ph.D. Thesis, Mechanical Engineering Department, University of Illinois at Urbana-Champaign, USA, 2000.

11. Sivaramakrishnan S., Bai H, Thomas B.G, Vanka S.P., Assar M. B., Dauby P.H., “*Transient Flow Structures in Continuous Casting of Steel*” 83rd Steelmaking Conference Proceedings, (Pittsburgh, PA, March 26-29, 2000), Vol. 83, Iron and Steel Society, Warrendale, PA, 2000.
12. Zhang Xing-guo, Zhang Wen-xiao, Jin Jun-ze, Evans J. W., “*Flow of Steel in Mold Region during Continuous Casting*” Journal of Iron and Steel Research, Intertional, 2007, 14(2): pp. 30-35, 41.
13. Kromhout J., “*Mould Powders for High Speed Continuous Casting of Steel*” Ph.D. Thesis, Department of Materials Science and Engineering, Delft University of Technology Delft, The Netherlands, 2011.
14. Thomas, B. G., “*Modeling of Continuous-Casting Defects Related to Mold Fluid Flow*”, 3rd Internat. Congress on Science & Technology of Steelmaking, Charlotte, NC, May 9-12, AIST, Warrendale, PA, 2005, pp. 847-861.
15. Zhang L., Yang S., Wang X., Cai K., Li J., Wan X., Thomas, B. G., “*Physical, Numerical and Industrial Investigation of Fluid Flow and Steel Cleanliness in the Continuous Casting Mold at Panzhihua Steel*” AISTech 2004, Nashville, TN, Sep.15-17, 2004. Assoc. IronSteel Technology, Warrendale, PA.
16. Chaudhary R., “*Studies of Turbulent Flows in Continuous Casting of Steel With and Without Magnetic Field*” Ph.D. Thesis, Mechanical Engineering Department, University of Illinois at Urbana-Champaign, USA, 2011.
17. Mizoguchi S., Ohashi T., Saeki T., “*Continuous Casting of Steel*”, Annual Review of Materials Science 1981, Volume 11 pp.151-169.
18. Thomas B.G., Dennisov A., Bai H., “*Behavior of Argon Bubbles during Continuous Casting of Steel*” ISS 80th Steelmaking Conference, Chicago, IL, ISS, April 13-16, 1997, Proceedings pp. 375-384.
19. Meadowcroft T.R., Milbourne R.J., “*A New Process for Continuously Casting Aluminum Killed Steel*”, Journal of Metals, June, 1971, pp. 11-17.

20. Shi T., “*Effect Of Argon Injection on Fluid Flow And Heat Transfer in The Continuous Slab Casting Mold*” Master Thesis, Mechanical Engineering Department, University of Illinois at Urbana-Champaign, USA.
21. Hsu C., Chung H., “*The Influence of Argon Flow on Inclusion Characteristic and Fatigue Life of Continuous Casting Bearing Steels*” Advanced Materials Research Vols. 418-420 (2012) pp. 972-976.
22. Degarmo E.P., Black J. T.; Kohser, R. A., “*Materials and Processes in Manufacturing (9th Ed.)*”, Wiley, p. 383, 2003.
23. Haissig M., “*Horizontal Continuous Casting - A Technology for the Future*”, Iron and Steel Engineer, Volume 61, pp. 65-70, 1984.
24. R. Hentrich, D. L. Sharma, D. Dittert and E. Roller, “*The Horizontal Casting of High-Alloy Steels Using the Krupp Oscillating Mold Process*”, Proc. 43rd Electric Arc Furnace Conference, TMS-AIME, Warrendale, PA, pp. 34-41, 1985.
25. Rietow B, Thomas B.G., “*Using Nail Board Experiments to Quantify Surface Velocity in the CC Mold*” AISTech 2008, Pittsburgh, PA, May 5-8, 2008.
26. Argyropoulos S. A., “*Measuring Velocity in High-Temperature Liquid Metals: A Review*” Scandinavian Journal of Metallurgy 2000; 30: 273–285.
27. Melissari B., Argyropoulos S. A. “*Measurement of Magnitude and Direction of Velocity in High-Temperature Liquid Metals. Part I: Mathematical Modeling*”, Metallurgical and Materials Transactions B, Volume 36b, October 2005, pp.691-700.
28. Yavuz, M. M., “*Liquid Steel Flow in Continuous Casting Machine: Modelling and Measurement*” Ironmaking and Steelmaking, Volume 38, No.6, pp. 453-463, 2011.

29. Meratian M., Hadjari A., “*Physical Modeling of Steel Delivery during Thin Slab Continuous Casting*” International Journal of ISSI, Vol. 5, 2008, No. 1, pp.41-46
30. Szekely J., Yadoya R. T., “*The Physical and Mathematical Modeling of the Flow Field in the Mold Region in Continuous Casting Systems: Part I. Model Studies With Aqueous Systems*” Metallurgical Transactions, October 1972, Volume 3, Issue 10, pp. 2673-2680.
31. Thomas B.G., “*Chapter. 3.9 Fundamentals of Continuous Casting: Modeling*”, Making Shaping & Treating of Steel, 11th Ed., A. Cramb, ed., AISE Steel Foundation, 2000.
32. Pericleous K., Djambazov G., Lebon B., Croft T. N., Domgin J. F., Gardin P., “*Time Dependent Modeling and Experimental Validation of the Metal/Flux Interface in a Continuous Casting Mould*”, Revue De Metallurgie Cahiers D’Informations Techniques 2008, Vol.105, pp. 33-43.
33. Tieu A. K., Kim I. S., “*Simulation of the Continuous Casting Process by a Mathematical Model*”, Int. J. Mech. Sci. Vol. 39, No. 2, pp. 185-192, 1997.
34. Vizag Steel, Continuous Casting Machine. [Photograph]. Retrieved April 26, 2014 from <http://www.vizagsteel.com/code/Infrastr/ccp.asp>.
35. Thomas, B.G., Vanka P., “*Study of Transient Flow Structures in the Continuous Casting of Steel*”, 2000 NSF Design & Manufacturing Grantees Conference, Vancouver, Canada, Jan. 5-8 2000, 14p.
36. Vesuvius, Stopper Rods. [Photograph]. Retrieved January 30, 2014 from <http://www.vesuvius.com/en-us/end-markets/iron-steel/casting/continuous-casting/tundish-flow-control-refractories/tundish-stoppers>.
37. Fedmet, Stopper Rods. [Photograph]. Retrieved January 30, 2014 from <http://www.fedmet.com/ag>.

38. Evertz Group, Copper Molds. [Photograph]. Retrieved October 30, 2013 from <http://www.evertz-group.com/en/companies/egon-evertz-kg/products-and-services/copper-moulds/>.
39. Omex Tech, Copper Molds. [Photograph]. Retrieved October 30, 2013 from <http://www.omextechchina.com/2011/11/23/copper-mould-tube/>
40. Yuan Q., Thomas, B.G., Vanka P., “*Turbulent Flow and Particle Motion in Continuous Slab-Casting Molds*” ISSTech 2003 (Conf. Proc.), Indianapolis, IN, USA, Apr. 27-30, 2003.
41. Iguchi M., Terauchi Y., “*Karman Vortex Probe for the Detection of Molten Metal Surface Flow in Low Velocity Range*” ISIJ International, Vol. 42 (2002), No. 9, pp. 939–943.
42. Hughes D. (2013, April, 1). Will Cheap Natural Gas Change Us Steel Production? *The Financialist*. Retrieved February 30, 2014 from <http://www.thefinancialist.com/will-cheap-natural-gas-change-us-steel-production/>.
43. Wilson N., Sun H. (2012, February, 21). Bluescope Steel Hot under the Collar, *Herald Sun Business*. <http://www.heraldsun.com.au/business/bluescope-steel-hot-under-the-collar/story-fn7j19iv-1226276404143>
44. SGT International, Steel Billet and Sheet. [Photograph]. Retrieved January 15, 2014 from <http://www.sgt-international.com/products.html>
45. Danieli, Steel Slabs. [Photograph]. Retrieved January 15, 2014 from <http://www.danieli.com/products/Continuous-Slab-Casters/Conventional-Slab-Casters/>
46. Munson B.R., Young D.F., Okiishi T.H., Huebsch W.W., “*Fundamentals of Fluid Mechanics (6th Ed.)*” John Wiley and Sons Inc., New York, 2009.

47. Fox R.W, McDonald A.T., "Introduction to Fluid Mechanics (6th Ed.)" John Wiley and Sons Inc., New York, 2003.
48. Incropera F.P, Dewitt D.P, Bergman T.L, Lavine A.S, "*Fundamentals of Heat and Mass Transfer (6th Ed.)*" Wiley, p. 949-, 2006.
49. Lei H., Zhu M. Y., He J.C., "*Mathematical and Physical Modeling of Interfacial Phenomena in Continuous Casting Mould with Argon Injection through Submerged Entry Nozzle*" Acta Metallurgical Sinica Vol. 13 No. 5 pp. 1079-1086 October 2000.
50. Thomas B.G., Bai H., Sivaramakrishnan S., Vanka S.P., "*Detailed Simulation of Flow in Continuous Casting of Steel using K- ϵ , LES, and PIV*" "International Symposium on Cutting Edge of Computer Simulation of Solidification and Processes", Osaka, Japan, Nov. 14-16, 1999, pp. 113-128.
51. Yuan Q., Sivaramakrishnan S., Vanka S.P., Thomas B.G., "*Computational and Experimental Study of Turbulent Flow in A 0.4-Scale Water Model of a Continuous Steel Caster*" Metallurgical and Materials Transactions B, October 2004, Volume 35, Issue 5, pp. 967-982.
52. Bai H., Thomas B.G., "*Turbulent Flow of Liquid Steel and Argon Bubbles in Slide-Gate Tundish Nozzles Part I: Model Development and Validation*" Metallurgical & Materials Transactions B, April 2001, Volume 32, Issue 2, pp. 253-267.
53. Szekely J., Wang H.J., Kiser K.M., "*Flow Pattern Velocity and Turbulence Energy Measurements and Predictions in a Water Model of an Argon-Stirred Ladle*" Metallurgical Transactions B, June 1976, Volume 7, Issue 2, pp. 287-295.
54. Bai H., Thomas B.G., "*Bubble Formation during Horizontal Gas Injection into Downward-Flowing Liquid*" Metallurgical and Materials Transactions B 32B, December 2001, pp: 1143 – 1159.

55. Yavuz, M. M., Cho, M. J., Lee, S. M. and Neale, K., “*Mold Flow Modeling of ArcelorMittal Riverdale and POSCO Thin Slab Casters*” AISTech 2010, May, Pittsburgh, Proceeding Volume 1 pp.1291-1302.
56. Yavuz, M. M., “*The Effects of Electromagnetic Brake on Liquid Steel Flow in Thin Slab Caster*” Steel Research International, Volume 82, Issue 7, July 2011, pp. 809-818.
57. Yuan Q., Thomas B.G., Vanka S.P., “*Study of Transient Flow and Particle Transport in Continuous Steel Caster Molds: Part I. Fluid Flow*” Metallurgical & Materials Transactions B, August 2004, Volume 35, Issue 4, pp. 685-702.
58. Yuan Q., Thomas B.G., Vanka S.P., “*Study of Transient Flow and Particle Transport in Continuous Steel Caster Molds: Part 2. Particle Transport*” Metallurgical & Materials Transactions B, August 2004, Volume 35, Issue 4, pp. 703-714.
59. Domgin J.F., Gardin P., Galpin J.M., “*Effect of Process Parameters Variation on CC Mould Hydrodynamics and Inclusions Behaviour*” La Revue de Métallurgie-CIT Octobre 2005.
60. Pericleous K., Kountouriotis Z., Djambazov G., Domgin J. F., Gardin P., “*Experimental and Numerical Simulation of the Mould Region of a Steel Continuous Caster*” International Conference of Numerical Analysis and Applied Mathematics 2010. AIP Conference Proceedings, Volume 1281, pp. 95-98.
61. Kountouriotis Z., “*Modeling of the Liquid Slag Behaviour in the Continuous Casting Mould*” Ph.D. Thesis, University of Greenwich, UK, 2011.
62. Gupta D., Lahiri A.K., “*Cold Model Study of the Surface Profile in a Continuous Slab Casting Mold: Effect of Second Phase*” Metallurgical and Materials Transactions B, August 1996, Volume 27, Issue 4, pp. 695-697.

63. Evans J. W., Xu D, Jones W K., “*Physical and Mathematical Modeling of Metal Flow in the Continuous Casting of Steel and Aluminum*” *Metals and Materials* December 1998, Volume 4, Issue 6, pp. 1111-1118.
64. Gutierrez-Montiel Y.S., Morales R.D., “*Control of Meniscus Stability in Medium Thickness-Straight Walls Slab Mould*” *ISIJ International*, Volume 53, 2013, No. 2, pp. 230–239.
65. Calderon-Ramos I., Barreto J.J., Garcia-Hernandez S., “*Physical and Mathematical Modelling of Liquid Steel Fluidynamics in a Billet Caster*” *ISIJ International*, Volume 53, 2013, No. 5, pp. 802–808.
66. Wang, Y.H., “3-D Mathematical Model Simulation on the Tundish Gate and Its Effect in the Continuous Casting Mold” *Iron and Steel Society*, Volume 75, 1992, pp. 271-278.
67. Cross M., Croft T.N., Djambazov G., Pericleous K. “Computational Modelling of Bubbles, Droplets and Particles in Metals Reduction and Refining” *Applied Mathematical Modelling*, Volume 30, pp. 1445-1458, 2006.
68. Creech, D., “Computational Modeling of Multiphase Turbulent Fluid Flow and Heat Transfer in the Continuous Slab Casting Mold” Master Thesis, Mechanical Engineering Department, University of Illinois at Urbana-Champaign, USA, 1999.
69. Hershey D. E., “*Turbulent Flow of Molten Steel Through Submerged Bifurcated Nozzles in the Continuous Casting Process*” Master Thesis, Mechanical Engineering Department, University of Illinois at Urbana-Champaign, USA, 1992.
70. Liu Z., Baokuan L., Maofa J., “*Transient Asymmetric Flow and Bubble Transport Inside a Slab Continuous-Casting Mold*” *Metallurgical and Materials Transactions B*, October 2013.

71. Yu H., Zhu M., Wang J., "Interfacial Fluctuation Behavior of Steel/Slag in Medium-Thin Slab Continuous Casting with Argon Gas Injection" *Journal of Iron and Steel Research*, International, 2011, 17(4): pp. 5-11.
72. Tsuge, H., "Hydrodynamics of Bubble Formation from Submerged Orifices," in *Encyclopedia of Fluid Mechanics*, vol. 3, (Houston, TX: Gulf Publishing Co., 1986), pp. 191-232.
73. Theodorakakos A. and Bergeles G. "*Numerical Investigation of the Interface in a Continuous Steel Casting Mold Water Model*" *Metallurgical and Materials Transactions B*, Volume 29B, December 1998, pp.1321-1327.
74. Panaras G.A., Theodorakakos A. and Bergeles G. "*Numerical Investigation of the Free Surface in a Continuous Steel Casting Mold Model*" *Metallurgical and Materials Transactions B*, Volume 29B, October 1998, pp.1117-1126.
75. Ansys Training Manual. Retrieved July 15, 2014 from <http://http://aerojet.engr.ucdavis.edu/fluenthelp/html/ug/node477.htm>

APPENDIX A

Jet Angle Calculation

Calculation of the overall jet angle:

$$U_i = \sqrt{u_i^2 + v_i^2 + w_i^2}$$

$$\bar{u} = \frac{\sum[u_i U_i]}{\sum[U_i]}, \quad \bar{v} = \frac{\sum[v_i U_i]}{\sum[U_i]},$$

$$\theta = \tan^{-1} \frac{\bar{v}}{\bar{u}}$$

In the above equations,

U_i is the liquid velocity at cell i of nozzle exit plane

\bar{u} is the average liquid velocity at nozzle port for x-direction

\bar{v} is the average liquid velocity at nozzle port for y-direction

θ is the overall jet angle

The summation operation, Σ , includes all velocity data at the port exit plane directed outwards.